

Measuring black hole masses from tidal disruption events and testing the $M_{\text{BH}}-\sigma_*$ relation

Z.Q. ZHOU ¹, F.K. LIU^{*},^{1,2} S. KOMOSSA,³ R. CAO,¹ L.C. HO,^{2,1} XIAN CHEN,^{1,2} AND SHUO LI^{4,1}

¹*Department of Astronomy, School of Physics, Peking University, Beijing 100871, China*

²*Kavli Institute for Astronomy and Astrophysics, Peking University, Beijing 100871, China*

³*Max Planck Institut für Radioastronomie, Auf dem Hügel 69, 53121 Bonn, Germany*

⁴*National Astronomical Observatories, Chinese Academy of Sciences, Beijing 100012, China*

ABSTRACT

Liu and collaborators recently proposed an elliptical accretion disk model for tidal disruption events (TDEs). They showed that the accretion disks of optical/UV TDEs are large and highly eccentric and suggested that the broad optical emission lines with complex and diverse profiles originate in a cool eccentric accretion disk of random inclination and orientation. In this paper, we calculate the radiation efficiency of the elliptical accretion disk and investigate the implications for observations of TDEs. We compile observational data for the peak bolometric luminosity and total radiation energy after peak brightness of 18 TDE sources and compare these data to the predictions from the elliptical accretion disk model. Our results show that the observations are consistent with the theoretical predictions and that the majority of the orbital energy of the stellar debris is advected into the black hole (BH) without being converted into radiation. Furthermore, we derive the masses of the disrupted stars and the masses of the BHs of the TDEs. The BH masses obtained in this paper are also consistent with those calculated with the $M_{\text{BH}}-\sigma_*$ relation. Our results provide an effective method for measuring the masses of BHs in large numbers of TDEs to be discovered in ongoing and next-generation sky surveys, regardless of whether the BHs are located at the centers of galactic nuclei or wander in disks and halos.

Keywords: accretion, accretion disk — black hole physics — galaxies: active — quasars: supermassive black holes — stars: black holes

1. INTRODUCTION

A star would be tidally disrupted (Hills 1975; Rees 1988; Evans & Kochanek 1989) when it is scattered close to the vicinity of a supermassive black hole (BH; Magorrian & Tremaine 1999; Wang & Merritt 2004; Chen et al. 2008, 2009; Liu & Chen 2013; Li et al. 2017). After the tidal disruption, about half of the stellar debris loses orbital energy and becomes bound to the BH. The bound stellar debris returns to the orbital pericenter of the progenitor star and forms an accretion disk around the BH. In the canonical model for such a tidal disruption event (TDE), the returned material streams are assumed to be circularized rapidly due to strong relativistic apsidal precession, and as a result, the accretion disk has a size of about twice the orbital

pericenter of the star (Rees 1988). In this scenario, the accretion disk of a TDE is an outer-truncated analog of an accretion disk of an active galactic nucleus (AGN) or Galactic X-ray binary, and it radiates mainly in the soft X-rays. The radiation in the optical and UV wave bands is expected to be rather weak and to decay with time as a power law much shallower than the fallback rate of the stellar debris (Strubbe & Quataert 2009). No strong broad optical emission lines are expected from such a hot accretion disk (Bogdanović et al. 2004).

The non-jetted TDEs discovered in the X-rays are broadly consistent with the above predictions, but those discovered in the optical/UV wave bands challenge the canonical model (Komossa & Bade 1999; Gezari et al. 2006; van Velzen et al. 2011; Liu et al. 2014; Komossa 2015, for a recent review). Most TDEs and candidate TDEs discovered in the optical/UV wave bands emit radiation mainly in optical/UV wave bands and little or no radiation in soft X-rays (e.g., Komossa et al. 2008; Gezari et al. 2012; Wang et al. 2012; Holoien et al. 2014, 2016a; Blagorodnova et al. 2019; Leloudas et al. 2019; van Velzen et al. 2020). Their optical/UV luminosities unexpectedly follow the fallback rate of the stellar debris (Gezari et al. 2012; Arcavi et al. 2014; Hung et al. 2017; Wevers et al. 2017; Mockler et al. 2019). The radiated energy and the implied accreted material onto the BH or the implied mass of the star could be orders of magnitude lower than expected for the tidal disruptions of main-sequence stars or brown dwarfs (Li et al. 2002; Halpern et al. 2004; Komossa et al. 2004; Esquej et al. 2008; Gezari et al. 2008, 2009; Cappelluti et al. 2009; Maksym et al. 2010; Gezari et al. 2012; Chornock et al. 2014; Donato et al. 2014; Holoien et al. 2014; Liu et al. 2014; Holoien et al. 2016a,b; Blagorodnova et al. 2017; Hung et al. 2017; Saxton et al. 2017, 2018; Mockler et al. 2019). Most optical/UV TDEs and candidate TDEs have strong broad optical emission lines with complex, asymmetric, and diverse profiles (Komossa et al. 2008; Gezari et al. 2012; Wang et al. 2012; Arcavi et al. 2014; Holoien et al. 2014, 2016a,b, 2019a).

It has recently been suggested that strong winds form during the phase of super-Eddington accretion, and that the soft X-ray radiation emitted by the accretion disk is absorbed and reprocessed into the UV band by the optically thick wind envelopes (e.g., Dai et al. 2018). The broad optical emission lines are powered by the soft X-rays and form in the surface layers of the optically thick envelopes (Roth et al. 2016). However, strong outflows may cause the observed light curve to diverge significantly from the fallback rate of stellar debris (Strubbe & Quataert 2009; Lodato & Rossi 2011; Metzger & Stone 2016).

Analytic and hydrodynamic simulations of stellar tidal disruptions (Rees 1988; Evans & Kochanek 1989; Kochanek 1994; Rosswog et al. 2009; Hayasaki et al. 2013, 2016; Guillochon et al. 2014; Dai et al. 2015; Piran et al. 2015; Shiokawa et al. 2015; Bonnerot et al. 2016; Sądowski et al. 2016; Bonnerot & Lu 2020) indicate that the bound stellar streams circularize mainly due to the self-interaction of the streams returning at different times caused by general relativistic apsidal precession. Rapid formation of the accretion disk happens only in TDEs with orbital pericenter $r_p \lesssim 10r_g$, with r_g the gravitational radius (Dai et al. 2015; Shiokawa et al. 2015; Bonnerot et al. 2016; Hayasaki et al. 2016). However, the tidal disruption radius of a solar-type star by a BH of mass $\lesssim 10^{6.5} M_\odot$ is $\gtrsim 10r_g$, so that the general relativistic apsidal precession of bound streams of most TDEs is expected to be inefficient in circularizing the streams (Shiokawa et al. 2015). Inspired by the hydrodynamic simulations of TDEs by Shiokawa et al. (2015), Piran et al. (2015) proposed that the observed luminosities of the optical/UV TDEs are powered by the orbital kinetic energy that is liberated by the self-crossing shocks at apocenter during the formation of the accretion disk rather than the energy released during the subsequent accretion of matter onto the BH. Because the self-collision of streams due to general relativistic apsidal precession occurs at nearly the apocenter of the most-bound stellar debris, the emission region could be much larger than that in the canonical circular disk model. The

observed luminosities and temperatures near peak brightness are roughly consistent with the expectations of the self-crossing shock model (Piran et al. 2015; Mockler et al. 2019), provided that the orbit of the fallback material is parabolic, with the specific bound energy much lower than that of the most-bound stellar debris, and so long as the dissipated kinetic energy is efficiently converted into radiation. As noted in the original work of Piran et al. (2015), a challenging question of the collision-shock model is where the energy goes that is liberated during the subsequent accretion of matter onto the BH. It is argued that the emissions during the formation of the accretion disk may dominate the radiation of TDEs because the eccentricity of the accretion disk may remain or even increase due to the efficient outward transfer of angular momentum by the self-crossing shocks and/or the magnetic stresses at apocenter, so that the gas pericenter could be reduced to the marginally stable orbit of the BH with little decrease in semimajor axis (Svirski et al. 2017; Chan et al. 2018).

It is generally believed that double-peaked broad Balmer emission lines in AGNs originate from their accretion disks (Chen & Halpern 1989; Chen et al. 1989; Storchi-Bergmann et al. 1993, 2017; Eracleous & Halpern 1994, 2003; Ho et al. 2000; Shields et al. 2000; Strateva et al. 2003; Popović et al. 2004). By modeling the double-peaked $H\alpha$ emission line of the optical/UV TDE PTF09djl, Liu et al. (2017) showed that the accretion disk is extended and extremely eccentric. The extreme eccentricity is determined jointly by the elliptical orbit of the most-bound stellar debris and the self-intersection of streams. Liu and collaborators further showed that the elliptical accretion disk model can also explain the broad optical emission lines in the TDE ASASSN-14li, and that the diversity and time variation of its lines are caused by the different inclination and orientation of the elliptical disk that is precessing due to the Lense–Thirring effect (Cao et al. 2018). Because of their large semimajor axis and extreme eccentricity, elliptical accretion disks have low conversion factors of matter into radiation (Liu et al. 2017; Cao et al. 2018), consistent with the radiation efficiencies obtained from the analysis of the light curves of PTF09djl and ASASSN-14li (Mockler et al. 2019). The expected peak energy luminosities from the elliptical disk model are also well consistent with the observations of PTF09djl and ASASSN-14li (Liu et al. 2017; Cao et al. 2018).

Here we further investigate the radiation efficiency of an elliptical accretion disk with a nearly uniform orbital eccentricity of the fluid elements in the disk plane, and we examine the implications for observations of TDEs. We assume that the outflows from the collision shocks during the formation of the accretion disk and from the surface of the elliptical accretion disk, if any, are a small fraction of the fallback stellar debris. Because we are interested in the total radiation efficiency, we do not distinguish between the emission of radiation from the collision shocks during the formation of the disk and from the subsequent accretion onto the disk. Within the framework of the elliptical accretion disk model, we calculate the conversion efficiency of matter into radiation of TDEs during the accretion of matter onto BHs, which in the literature is always assumed to be a free parameter in modeling the luminosities of TDEs (e.g., Liu et al. 2014; Mockler et al. 2019). With the radiation efficiency, we can calculate the expected peak luminosity and total radiation energy of TDEs and compare the expectations with the observations of non-jetted TDEs in the literature. We show that the peak luminosity and the total radiation energy expected from an elliptical accretion disk are well consistent with the observations of the non-jetted TDEs and candidate TDEs.

In the elliptical accretion disk model for a Schwarzschild BH, the radiation efficiency is not a constant but depends significantly on the mass of the BH and the mass of the star. With the observations of the peak luminosity and the total radiation energy of non-jetted TDEs, we can derive the masses of the BHs and the disrupted stars. This provides a potentially promising method for constraining the masses of tidally disrupted stars in distant galaxies. Because the masses of BHs in galactic nuclei can be estimated from well-

known correlations between BH mass and host galaxy properties, we show that the BH masses obtained in this paper are consistent with those calculated from the $M_{\text{BH}}-\sigma_*$ relation. This paper provides an effective technique to weigh both the BHs and the stars disrupted by them, regardless of whether they hide deep in the center of galactic nuclei and globular clusters or wander around the galactic disk.

The paper is organized as follows. Section 2 presents the elliptical disk model for TDEs and calculates the radiation efficiency. Section 3 gives the peak luminosity and the total radiation energy after peak. In Section 4 we compile the observational data of the peak bolometric luminosity and the total radiation energy after peak brightness of 18 non-jetted TDEs and compare the observations with the predictions of the elliptical disk model. In Section 5 we calculate the masses of BHs and stars according to the peak luminosity and the total radiation energy after peak, and compare the results with those obtained from the correlation between BH mass and bulge properties. Discussion is presented in Section 6, and conclusions can be found in Section 7.

2. ELLIPTICAL ACCRETION DISK AND RADIATION EFFICIENCY OF TDES

We begin our calculation of the radiative efficiency by introducing our elliptical accretion disk model of TDEs. A star is tidally destroyed when it passes by a supermassive BH with an orbital pericenter r_p smaller than the tidal disruption radius,

$$r_t = R_* (M_{\text{BH}}/M_*)^{1/3} \simeq 23.557 r_* m_*^{-1/3} M_6^{-2/3} r_S, \quad (1)$$

where $M_{\text{BH}} = 10^6 M_6 M_\odot$ is the mass of the BH, r_S is the BH Schwarzschild radius, and $R_* = r_* R_\odot$ and $M_* = m_* M_\odot$ are the stellar radius and mass, respectively. Hydrodynamic simulations of TDEs show that the tidal disruption radius depends on both the internal structure of the star and general relativistic effects of the BH (Guillochon & Ramirez-Ruiz 2013; Ryu et al. 2020a,b). The result given by Equation (1) is an approximation with an uncertainty of order unity. For a star with an orbital penetration factor $\beta = r_t/r_p$ and a BH of mass $M_{\text{BH}} = 10^6 M_6 M_\odot$, the physical tidal disruption corresponds to $\beta \sim 0.9$ for low-mass main-sequence stars and $\beta \sim 2$ for stars with $M_* > 1 M_\odot$ (Guillochon & Ramirez-Ruiz 2013; Ryu et al. 2020b). In this paper, if needed, we calculate the radius with the mass-radius relation $R_* \simeq R_\odot (M_*/M_\odot)^{1-\zeta}$ for main-sequence stars, where $\zeta \simeq 0.21$ for stellar masses $0.08 M_\odot < M_* \leq 1 M_\odot$ and $\zeta \simeq 0.44$ for $1 M_\odot < M_* < 150 M_\odot$ (Kippenhahn et al. 2012). In the literature, hydrodynamic simulations of tidal disruptions have mainly been made with main-sequence stars. Here we extrapolate the results of main-sequence stars to brown dwarfs (BDs) using the same polytropic index. We note that the results with BDs have larger uncertainties. For BDs with mass $0.01 M_\odot < M_* \leq 0.07 M_\odot$, we use the mass-radius relation appropriate for an age $t = 5 \text{ Gyr}$, $R_* \simeq 0.06 R_\odot (M_*/M_\odot)^{1-\zeta}$ with $\zeta = 9/8$ (Chabrier & Baraffe 2000). For BDs with mass $0.07 M_\odot < M_* < 0.08 M_\odot$, we adopt a bridge relation $R_* = 0.136 R_\odot (M_*/0.08 M_\odot)^{1-\zeta}$ with $\zeta = -2.637$.

After tidal disruption, the bound stellar debris returns to the pericenter of the progenitor star and forms an accretion disk mainly due to the shock produced by the collision between the post-pericenter outflowing and the freshly inflowing streams that results from relativistic apsidal precession (Evans & Kochanek 1989; Kochanek 1994; Hayasaki et al. 2013; Dai et al. 2015; Shiokawa et al. 2015; Bonnerot et al. 2016; Hayasaki et al. 2016). The location of the collision and the conservation of angular momentum together determine the semimajor axis of the disk (Dai et al. 2015; Liu et al. 2017; Cao et al. 2018),

$$a_d \simeq \frac{2r_p}{2\delta + \sin^2(\Omega/2)} \simeq \frac{2\beta^{-1}r_t}{2\delta + \sin^2(\Omega/2)}, \quad (2)$$

as well as the eccentricity,

$$e_d \simeq \left[1 - \frac{(1 - e_{\text{mb}}^2) a_{\text{mb}}}{a_d} \right]^{1/2} \simeq \left[1 - 2\delta - \sin^2 \left(\frac{\Omega}{2} \right) \right]^{1/2} \simeq [1 - 2\delta(1 + \Delta)]^{1/2}, \quad (3)$$

with $\Delta = \sin^2(\Omega/2)/(2\delta)$. In Equation (3), $a_{\text{mb}} \simeq r_t^2/2R_*$ and $e_{\text{mb}} = 1 - \delta$ with $\delta \simeq 2R_*r_p/r_t^2 \simeq 0.02\beta^{-1}m_*^{1/3}M_6^{-1/3}$ are the orbital semimajor axis and eccentricity, respectively, of the most-bound stellar debris. The instantaneous de Sitter precession at periape of the most-bound stellar debris is

$$\Omega \simeq \frac{6\pi GM_{\text{BH}}}{c^2(1 - e_{\text{mb}}^2)a_{\text{mb}}} \simeq \frac{3\pi r_s}{(1 + e_{\text{mb}})r_p} \simeq \frac{3\pi}{2 - \delta} \beta \frac{r_s}{r_t}. \quad (4)$$

For a star with an orbital pericenter of $r_p < 10r_g$, the relativistic apsidal precession of the bound stellar debris becomes important and would significantly reduce the eccentricity of the accretion disk.

Modeling of the double-peaked and/or asymmetric broad optical emission lines of TDEs implies that the accretion disks of TDEs are highly eccentric and that the eccentricity remains nearly unchanged over the disk (Liu et al. 2017; Cao et al. 2018). This result suggests that stellar streams circularize inefficiently. Analytical arguments as well as numerical hydrodynamic simulations also show that the accretion disks of TDEs can be highly eccentric (Guillochon et al. 2014; Shiokawa et al. 2015; Barker & Ogilvie 2016; Sądowski et al. 2016; Svirski et al. 2017; Chan et al. 2018; Ogilvie & Lynch 2019; Andalman et al. 2020; Bonnerot & Lu 2020). Recent global general relativistic hydrodynamic simulations indicate that the average eccentricity of TDE disks can be $e \simeq 0.88$ at late times (Andalman et al. 2020), consistent with the modeling of the observed line profiles (Liu et al. 2017; Cao et al. 2018). Following Liu et al. (2017) and Cao et al. (2018), and for simplicity, we assume that the eccentricity of the elliptical accretion disks of TDEs is nearly uniform over the disk, namely $e(a) \simeq e_d$. To describe the motion of the particles of highly eccentric orbits in the field of a Schwarzschild BH, we adopt the generalized Newtonian potential in the low-energy limit (gNR; Tejeda & Rosswog 2013),

$$\Phi_G = -\frac{GM_{\text{BH}}}{r} - \left(\frac{2r_g}{r - 2r_g} \right) \left[\left(\frac{r - r_g}{r - 2r_g} \right) v_r^2 + \frac{1}{2} v_\phi^2 \right], \quad (5)$$

where r_g is the gravitational radius, v_r is the radial velocity, and v_ϕ is the azimuthal velocity. In gNR, the specific binding energy e_G and angular momentum l_G of an elliptical orbit with semimajor axis a and eccentricity e_d are

$$e_G \simeq \frac{c^2}{2} \frac{r_s [a(1 - e_d^2) - 2r_s]}{a [2a(1 - e_d^2) - (3 + e_d^2)r_s]} \quad (6)$$

and

$$l_G \simeq \frac{(1 - e_d^2)ac\sqrt{r_s}}{\sqrt{2(1 - e_d^2)a - (3 + e_d^2)r_s}}, \quad (7)$$

respectively (Liu et al. 2017; Cao et al. 2018).

When the disk fluid elements migrate inward until the pericenter reaches the marginally stable radius r_{ms} , the matter passes through r_{ms} and falls freely onto the BH. We adopt the innermost elliptical orbit of the fluid elements as the inner edge of the elliptical accretion disk and take the zero-torque inner boundary

condition. It has been argued that if the magnetohydrodynamic turbulence around the pericenter develops in the usual way, the viscous time of the elliptical accretion disk would be very long and the accretion of matter onto the BH would be delayed (Shiokawa et al. 2015). However, the magnetorotational instability may develop differently in an eccentric accretion disk (Chan et al. 2018). Both the shocks due to relativistic apsidal precession and the magnetic stresses near apocenter can transport angular momentum outward and efficiently reduce the gas pericenter (Bonnerot et al. 2017; Svirski et al. 2017). Nealon et al. (2018) propose that gas accretion at early times can be produced by angular momentum associated with the Papaloizou & Pringle (1984) instability. If the accretion time of an elliptical accretion disk is short compared to the evolutionary time of the TDE, the radiative efficiency can be calculated from the energy liberated by the particles on the elliptical orbit of the inner edge.

An elliptical accretion disk of constant eccentricity e_d has an inner edge $a_{\text{in}} = r_{\text{ms}}/(1 - e_d)$. For particles on circular orbits, the marginally stable circular orbit or the innermost stable circular orbit (ISCO) is at $r_{\text{ms}} = 3r_s$, while for particles with parabolic orbits, the marginally stable radius is at $r_{\text{ms}} = 2r_s$. Particles with trajectories of eccentricity $0 < e < 1$ are characterized by $2r_s < r_{\text{ms}} < 3r_s$. Provided r_{ms} , Equation (6) gives the specific binding energy ϵ_{in} of particles at the inner edge of the elliptical disk, and the conversion efficiency of matter into radiation is

$$\eta = \frac{\Delta\epsilon_G}{c^2} = \frac{\epsilon_{\text{in}} - \epsilon_{\text{init}}}{c^2} \simeq \frac{\epsilon_{\text{in}}}{c^2} \simeq \frac{1}{2} \frac{r_s[(1 + e_d)r_{\text{ms}} - 2r_s](1 - e_d^2)}{(1 + e_d)r_{\text{ms}}[2(1 + e_d)r_{\text{ms}} - (3 + e_d^2)r_s]}, \quad (8)$$

where ϵ_{init} is the initial specific binding energy of the inflowing bound stellar debris. Because the initial specific binding energy of the inflowing stellar debris is $0 < \epsilon_{\text{init}} \leq \epsilon_{\text{mb}} \ll \epsilon_{\text{in}}$, with $\epsilon_{\text{mb}} \simeq GM_{\text{BH}}R_*/r_t^2$ the specific binding energy of the most-bound stellar debris, we have $\Delta\epsilon_G = \epsilon_{\text{in}} - \epsilon_{\text{init}} \simeq \epsilon_{\text{in}}$. For $e_d = 1$ and $r_{\text{ms}} = 2r_s$, Equation (8) gives $\eta = 0$, as expected for a parabolic orbit. For $e_d = 0$ and $r_{\text{ms}} = 3r_s$, Equation (8) gives $\eta \simeq 1/18$, which is about 2.9% smaller than the exact value of $\eta \simeq 0.0572$. From Equations (8) and (3), we have

$$\eta \simeq \eta_0(1 - e_d^2) \simeq \eta_0 \left[2\delta + \sin^2 \left(\frac{\Omega}{2} \right) \right] = 2\eta_0\delta(1 + \Delta), \quad (9)$$

with $\Delta = \sin^2(\Omega/2)/2\delta$, where

$$\eta_0 = \frac{1}{2} \frac{r_s[(1 + e_d)r_{\text{ms}} - 2r_s]}{(1 + e_d)r_{\text{ms}}[2(1 + e_d)r_{\text{ms}} - (3 + e_d^2)r_s]} \quad (10)$$

depends very weakly on both r_{ms} and e_d . For $e_d = 1$ and $r_{\text{ms}} = 2r_s$, $\eta_0 = 0.0625$, while $\eta_0 = 0.0556$ for $e_d = 0$ and $r_{\text{ms}} = 3r_s$. Adopting an average of $\eta_0 = 0.059$ yields a good approximation for calculating the radiation efficiency with Equation (9). In particular, for $r_p \gg r_s$ we have

$$\eta \simeq 2.36 \times 10^{-3} \left(\frac{\eta_0}{0.059} \right) (1 + \Delta) \beta^{-1} m_*^{1/3} M_6^{-1/3} \quad (11)$$

and $\Delta \simeq 0.25\beta^3 r_*^{-2} m_*^{1/3} M_6^{5/3}$.

To estimate η_0 with higher accuracy, we calculate the marginally stable radius r_{ms} with the eccentricity given by Equation (3). From Equation (7), the angular momentum of the fluid elements of the disk inner edge with eccentricity e_d is approximately

$$l_{\text{in}} \simeq \frac{(1 + e_d)r_{\text{ms}}c\sqrt{r_s}}{\sqrt{2(1 + e_d)r_{\text{ms}} - (3 + e_d^2)r_s}}. \quad (12)$$

For fluid elements with specific angular momentum l_{in} , the marginally stable radius is given by

$$l_{\text{in}} = l_{\text{K}} \quad (13)$$

(Abramowicz et al. 1978), where

$$l_{\text{K}} = \Omega_{\text{K}} \frac{r_{\text{ms}}^3}{r_{\text{ms}} - r_{\text{S}}} \quad (14)$$

is the specific angular momentum of Keplerian circular motion and $\Omega_{\text{K}} = (GM_{\text{BH}}/r_{\text{ms}}^3)^{1/2}$ is the Keplerian angular velocity. From Equations (12)–(14), we obtain

$$r_{\text{ms}} = \frac{A}{4(1+e_{\text{d}})e_{\text{d}}} r_{\text{S}}, \quad (15)$$

where $A = 1 + 8e_{\text{d}} + 3e_{\text{d}}^2 + \sqrt{1 + 22e_{\text{d}}^2 - 7e_{\text{d}}^4}$ increases with decreasing eccentricity. For $e_{\text{d}} = 1$, Equation (15) give $r_{\text{ms}} = 2r_{\text{S}}$, consistent with the marginally bound radius of parabolic orbits. When $e_{\text{d}} \leq 0.406$, Equation (15) gives $r_{\text{ms}} \geq 3r_{\text{S}}$. In the following calculation of the efficiency η , $r_{\text{ms}} = 3r_{\text{S}}$ is adopted for eccentricity $e_{\text{d}} \leq 0.406$.

We note that in Equation (9), $\eta_0 \simeq 0.059$ is close to the radiation efficiency of a standard thin accretion disk around a Schwarzschild BH, and the radiation efficiency η of the elliptical accretion disk of TDEs is equivalent to the typical radiation efficiency of a standard thin accretion disk modified by a factor $(1 - e^2)$. Equation (9) shows that the radiation efficiency of the elliptical accretion disk of TDEs strongly depends both on the masses of the BH and star and on the orbital penetration factor of the star. Figure 1 shows the variation in η as a function of the masses of the BH and star for two typical orbital penetration factors, $\beta = 1$ and 2. Figure 1 assumes the mass-radius relations of main-sequence stars and BDs.

The total radiation energy of the elliptical accretion disk partly comes from the self-crossing shocks near the disk apocenter during disk formation and partly from the subsequent accretion of matter onto the BH. Assuming that the heat of the shock is completely radiated away (e.g., Piran et al. 2015; Wevers et al. 2019b), we can estimate the maximum radiation efficiency η_{sh} of the self-crossing shocks as

$$\begin{aligned} \eta_{\text{sh}} &\simeq \frac{\epsilon_{\text{d}} - \epsilon_{\text{init}}}{c^2} \\ &\simeq \frac{1}{8} \frac{r_{\text{S}}}{r_{\text{p}}} \frac{(r_{\text{p}} - r_{\text{S}}) [2\delta + \sin^2(\Omega/2)]}{(r_{\text{p}} - r_{\text{S}}) + \frac{r_{\text{S}}}{4} [2\delta + \sin^2(\Omega/2)]} - \frac{\epsilon_{\text{init}}}{c^2} \\ &\simeq \frac{1}{8} \frac{r_{\text{S}}}{r_{\text{t}}} \beta \left[2\delta + \sin^2\left(\frac{\Omega}{2}\right) \right] - \frac{\epsilon_{\text{init}}}{c^2} \\ &\simeq 5.31 \times 10^{-3} \beta r_{*}^{-1} m_{*}^{1/3} M_6^{2/3} \left[2\delta + \sin^2\left(\frac{\Omega}{2}\right) \right] - \frac{\epsilon_{\text{init}}}{c^2} \\ &\simeq 2.12 \times 10^{-4} r_{*}^{-1} m_{*}^{2/3} M_6^{1/3} (1 + \Delta) - \frac{\epsilon_{\text{init}}}{c^2}. \end{aligned} \quad (16)$$

In earlier works on the self-crossing shock model for optical TDEs (e.g., Piran et al. 2015; Jiang et al. 2016; Wevers et al. 2019b), an initial parabolic orbit is adopted for the inflowing stream so that the initial specific orbital energy is $\epsilon_{\text{init}} = 0$. This approximation is valid for the orbits of the inflowing streams at late times, but it is inadequate for orbits near the peak fallback rate, whose initial orbital binding energy is similar to that of the most-bound stellar debris ($\epsilon_{\text{init}} \simeq \epsilon_{\text{mb}}$). Figure 1(b) illustrates η_{sh} for $\epsilon_{\text{init}} \simeq \epsilon_{\text{mb}}$ and $\epsilon_{\text{init}} \simeq 0$. The case of $\epsilon_{\text{init}} \simeq 0$ (dash-dotted lines) represents the upper limits of the radiation efficiency of the self-crossing shocks

at apocenter. The radiation efficiencies of the self-crossing shocks at the peak fallback rate are expected to closely follow the curves for $\epsilon_{\text{init}} \simeq \epsilon_{\text{mb}}$ (solid and dashed lines). The radiation efficiency η_{d} of the disk during the subsequent accretion of matter onto the BH can be estimated by

$$\begin{aligned} \eta_{\text{d}} &\simeq \frac{\eta - \eta_{\text{sh}}}{\epsilon_{\text{in}} - \epsilon_{\text{d}}} \\ &\simeq \frac{c^2}{c^2} \\ &\simeq \left(1 - \frac{1}{8} \frac{r_{\text{s}}}{r_{\text{t}}} \frac{\beta}{\eta_0}\right) \eta_0 \left[2\delta + \sin^2\left(\frac{\Omega}{2}\right)\right] \\ &\simeq \eta \left[1 - 0.09 \beta r_*^{-1} m_*^{1/3} M_6^{2/3} \left(\frac{\eta_0}{0.059}\right)^{-1}\right]. \end{aligned} \quad (17)$$

Equation (17) gives the lower limit of the radiation efficiency during the subsequent accretion of matter onto the BH because most of the heat energy of the self-crossing shocks at the apocenter would be converted back into the internal kinetic energy during the adiabatic expansion of the downstream gas (Jiang et al. 2016). Equation (17) and Figure 1(c) show that for BHs with $M_{\text{BH}} \sim 10^7 M_{\odot}$, $\eta_{\text{d}} \sim \eta_{\text{sh}}$. For BHs with $M_{\text{BH}} = 10^6 M_{\odot}$ and $\beta \sim 1$, $\eta \simeq \eta_{\text{d}} \gg \eta_{\text{sh}}$, and the total luminosity is dominated by the radiation of the elliptical accretion disk.

For comparison, Figure 1 also plots the radiation efficiency $\eta = 0.1$ that is typically adopted for TDEs and AGNs. The total and disk radiation efficiencies change little with the initial binding energy of the stellar debris, while Figure 1(b) shows that the radiation efficiency of the self-crossing shocks varies significantly. Our results are based on the total radiation efficiency and do not change significantly with the assumption of $\epsilon_{\text{init}} \sim 0$. The figure further shows that the total radiation efficiency η is a convex function of BH mass, with a minimum as low as $\eta \sim 10^{-3}$ at $M_{\text{BH}} \approx 10^6 M_{\odot} - 10^7 M_{\odot}$. The radiation efficiency of an elliptical accretion disk is significantly lower than $\eta = 0.1$. The radiation efficiency during the accretion of matter onto the BH is always significant, while the radiation efficiency η_{sh} of the self-crossing shocks at the time of disk formation increases with BH mass and becomes important when the relativistic apsidal precession is strong for high BH masses.

3. PEAK LUMINOSITIES AND TOTAL RADIATION ENERGY AFTER PEAK

The peak luminosities and the total radiation energies of TDEs can be determined observationally. We calculate these quantities according to the elliptical accretion disk model in this section and compare them to the observations of TDEs in the next section.

Analytic and hydrodynamic simulations of TDEs show that the fallback rate of the bound stellar debris after peak can be well approximated with a power law in time

$$\dot{M} \simeq \dot{M}_{\text{p}} \left(\frac{t - t_{\text{d}}}{t_{\text{p}} - t_{\text{d}}}\right)^{-n}, \quad (18)$$

where t_{d} and t_{p} are the time of tidal disruption and peak mass accretion rate, respectively. In Equation (18), the power-law index of the typical value $n = 5/3$ is a constant that depends on the structure and age of the star (Lodato et al. 2009; Guillochon & Ramirez-Ruiz 2013; Goicovic et al. 2019; Golightly et al. 2019; Law-Smith et al. 2019; Ryu et al. 2020b), and the peak mass fallback rate

$$\dot{M}_{\text{p}} \simeq A_{\gamma} r_*^{-3/2} m_*^2 M_6^{-1/2} M_{\odot} / \text{yr}, \quad (19)$$

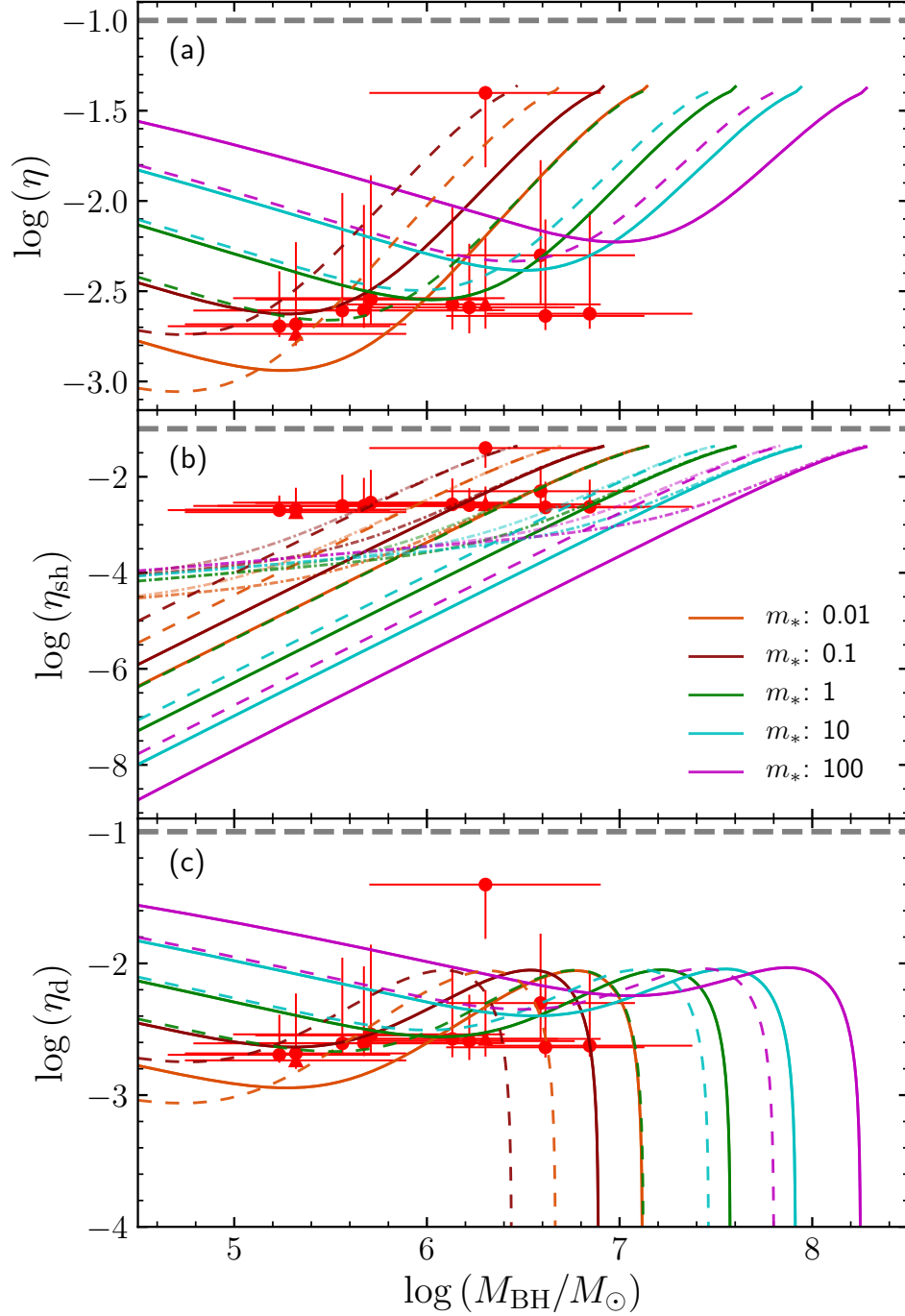


Figure 1. Radiation efficiency vs. BH mass for different stellar masses for (a) the total radiation efficiency η , (b) the radiation efficiency η_{sh} of the self-crossing shocks at apocenter, and (c) the radiation efficiency η_d during the subsequent accretion of matter onto the BH. The solid ($\beta = 1$) and dashed ($\beta = 2$) lines are for an initial orbital bound energy $\epsilon_{\text{init}} = \epsilon_{\text{mb}}$, and the dash-dotted lines ($\beta = 1$ and 2) in panel (b) are for an initial parabolic orbit $\epsilon_{\text{init}} = 0$. Gray dashed lines are for $\eta = 0.1$. The filled circles are the radiation efficiencies and the associated uncertainties at 90% level of the sample of TDE sources in Table 2. The triangles are for the secondary solutions of TDEs (see Section 4.3 for details).

where A_γ is a constant that depends on the penetration factor β and the structure and age of the star (Lodato et al. 2009; Guillochon & Ramirez-Ruiz 2013; Goicovic et al. 2019; Golightly et al. 2019; Law-Smith et al. 2019; Ryu et al. 2020b) and weakly on the mass of the BH (Ryu et al. 2020a). For full tidal disruptions, n is typically 5/3, especially for the fallback rate at late times (Rees 1988; Evans & Kochanek 1989; Lodato et al. 2009; Stone et al. 2013). For partial disruptions, n is well approximated with 9/4 (Guillochon & Ramirez-Ruiz 2013; Coughlin & Nixon 2019; Ryu et al. 2020c). In this work, we adopt the typical value $n = 5/3$, and the results are not significantly changed with different values of n . For the tidal disruption of a solar-type star with a polytropic index $\gamma = 5/3$ and a penetration factor $\beta = 1$, we have $n \simeq 5/3$ and $A_{5/3} \simeq 1.328$ (Guillochon & Ramirez-Ruiz 2013), which we used to scale the peak fallback rate as required. For other stars, we use the results of hydrodynamic simulations of polytropic stars (Guillochon & Ramirez-Ruiz 2013). We adopted $\gamma = 5/3$ both for BDs with masses between $0.01 M_\odot$ and $0.08 M_\odot$ (Chabrier & Baraffe 2000) and for low-mass main-sequence stars with masses between $0.08 M_\odot$ and $1 M_\odot$. We use $\gamma = 4/3$ for high-mass stars with $M_* > 20 M_\odot$, whereas for stars with $1 M_\odot < M_* < 20 M_\odot$, we use a hybrid model obtained by linearly interpolating the results of hydrodynamic simulations of polytropes with indices $\gamma = 5/3$ and $\gamma = 4/3$. No hydrodynamic simulations of the tidal disruptions of BDs have been carried out so far, although general relativistic hydrodynamic simulations have been carried out for a red dwarf on an eccentric orbit (Sądowski et al. 2016). Because the degeneracy of electron gas affects the equation-of-state of BDs and a degenerate electron gas can be described by polytropes of $\gamma = 5/3$ (Chabrier & Baraffe 2000), we extrapolate the results of the low-mass stars with $\gamma = 5/3$ to obtain the peak fallback rate for BDs (Guillochon & Ramirez-Ruiz 2013).

For the typical radiation efficiency $\eta = 0.1$ of a circular accretion disk, Equation (19) gives the peak luminosity

$$\begin{aligned} L_p &= \eta \dot{M}_p c^2 \\ &\simeq 7.53 \times 10^{45} \text{ erg s}^{-1} \left(\frac{\eta}{0.1} \right) \left(\frac{A_\gamma}{1.328} \right) M_6^{-1/2} r_*^{-3/2} m_*^2 \\ &\simeq 60 L_{\text{Edd}} \left(\frac{\eta}{0.1} \right) \left(\frac{A_\gamma}{1.328} \right) M_6^{-3/2} r_*^{-3/2} m_*^2 \end{aligned} \quad (20)$$

with $L_{\text{Edd}} = 1.25 \times 10^{44} M_6 \text{ erg s}^{-1}$ being the Eddington luminosity. Although L_{Edd} is independent of η , the Eddington accretion rate depends on η , as $\dot{M}_{\text{Edd}} = L_{\text{Edd}}/\eta c^2 = 0.022 \eta_{-1}^{-1} M_6 M_\odot \text{ yr}^{-1} = 2.2 \eta_{-3}^{-1} M_6 M_\odot \text{ yr}^{-1}$, where $\eta_{-1} = \eta/0.1$ and $\eta_{-3} = \eta/10^{-3}$. For the value of $\eta = 0.1$ that is typically adopted for TDEs in the literature, the peak luminosity in Equation (20) becomes super-Eddington for BHs of mass $M_{\text{BH}} \lesssim 1.5 \times 10^7 (A_\gamma/1.328)^{2/3} r_*^{-1} m_*^{4/3} M_\odot$. Because the peak luminosity is highly super-Eddington, the light curves of TDEs for BHs of $M_{\text{BH}} \sim 10^6 M_\odot$ are Eddington-limited and should deviate from the fallback rate given by Equation (18). For a radiation efficiency as low as $\eta = 10^{-3}$, Equation (20) shows that the peak luminosity is sub-Eddington with $L_p \simeq 0.6 L_{\text{Edd}}$, even for $M_{\text{BH}} \sim 10^6 M_\odot$.

For the elliptical accretion disk with the efficiency given by Equation (9), the peak luminosity of TDEs is

$$\begin{aligned} L_p &= \eta \dot{M}_p c^2 \\ &= \eta_0 A_\gamma \left[2\delta + \sin^2 \left(\frac{\Omega}{2} \right) \right] r_*^{-3/2} m_*^2 M_6^{-1/2} c^2 M_\odot / \text{yr} \\ &\simeq 1.78 \times 10^{44} \text{ erg s}^{-1} \left(\frac{\eta_0}{0.059} \right) \left(\frac{A_\gamma}{1.328} \right) \beta^{-1} r_*^{-3/2} m_*^{7/3} M_6^{-5/6} \times \\ &\quad \left(1 + 0.25 \beta^3 r_*^{-2} m_*^{1/3} M_6^{5/3} \right). \end{aligned} \quad (21)$$

In Equation (21), the last equality is valid for $r_p \gg r_s$. Equation (21) shows that the peak luminosity of TDEs is sub-Eddington for BH masses $M_{\text{BH}} \gtrsim 10^6 M_\odot$. The peak luminosity is significantly super-Eddington, and a significant Eddington-limited plateau of the peak brightness is expected only for those TDEs with $M_{\text{BH}} \ll 1 \times 10^6 M_\odot (\eta_0/0.059)^{6/11} (A_\gamma/1.328)^{6/11} \beta^{-6/11} r_*^{-9/11} m_*^{14/11}$, about an order of magnitude smaller than that suggested by Equation (20). When the disrupted star is a late-type M dwarf with a typical mass $m_* \simeq 0.3$, the peak accretion rate is super-Eddington only for $M_{\text{BH}} \lesssim 5.7 \times 10^5 M_\odot (\eta_0/0.059)^{6/11} (A_\gamma/1.328)^{6/11} \beta^{-6/11}$. For BHs more massive than $M_{\text{BH}} \approx 10^6 M_\odot$, producing a TDE with significantly super-Eddington luminosity requires that the disrupted star is of B or O type. Our results predict that TDEs whose light curves clearly show Eddington-limited plateaus would predominantly occur in either dwarf galaxies with intermediate-mass BHs ($M_{\text{BH}} \lesssim 10^5 M_\odot$) or star-forming galaxies rich in massive O-type stars.

According to Equation (20), in a circular accretion disk the peak luminosity increases with BH mass as $L_p \sim L_{\text{Edd}} \propto M_{\text{BH}}$ for $M_{\text{BH}} \lesssim 2 \times 10^7 M_\odot$ because of the Eddington limit and decreases with BH mass as $L_p \propto M_{\text{BH}}^{-1/2}$ for $M_{\text{BH}} \gtrsim 2 \times 10^7 M_\odot$. A peak in the distribution of the peak luminosity is expected at $M_{\text{BH}} \sim 2 \times 10^7 M_\odot$. By contrast, for an elliptical disk (Equation (21)) $L_p \propto M_{\text{BH}}^{-5/6}$ for $M_{\text{BH}} \lesssim 2 \times 10^6 M_\odot \beta^{-9/5} r_*^{6/5} m_*^{-1/5}$ and $L_p \propto M_{\text{BH}}^{5/6}$ for $M_{\text{BH}} \gtrsim 3 \times 10^6 M_\odot \beta^{-9/5} r_*^{6/5} m_*^{-1/5}$. Figure 2a illustrates the dependence of the expected peak luminosity of an elliptical disk as a function of BH and stellar mass for a penetration factor $\beta = 1$. A minimum in the distribution of L_p is prominent in Figure 2, and the BH mass at the minimum increases with stellar mass for main-sequence stars and decreases with stellar mass for BDs. We have used the mass-radius relations to obtain Figure 2, with the mass range for different types of stars taken from Cox (2000). Figure 2 shows that the peak luminosities of TDEs strongly depend on both the mass of the BH and the mass of the star. They increase monotonically with star mass except at the transitions from BDs to late M-type main-sequence stars, and from F-type to early O-type main-sequence stars. Figure 2 also plots the peak luminosity as a function of BH mass given by Equation (20) for $\eta = 0.1$ and $M_* = 1 M_\odot$. This shows that for TDEs with solar-type stars the peak luminosities predicted by the popular circular accretion disk model are typically orders of magnitudes higher than those of the elliptical accretion disk model.

From Equation (18), the total fallback and accreted mass after peak time t_p is

$$\begin{aligned} \Delta M_* &\simeq \int_{t_p}^{\infty} \dot{M}_p \left(\frac{t-t_d}{t_p-t_d} \right)^{-n} dt \simeq \frac{\dot{M}_p}{n-1} \Delta t_p \\ &\simeq \frac{A_\gamma B_\gamma}{n-1} m_* M_\odot \simeq \frac{3}{2} A_\gamma B_\gamma m_* M_\odot, \end{aligned} \quad (22)$$

where $\Delta t_p = t_p - t_d \simeq B_\gamma M_6^{1/2} m_*^{-1} r_*^{3/2}$ yr is the time of peak accretion and B_γ is a constant depending on the polytropic index γ and the orbital penetration factor β of the star (Guillochon & Ramirez-Ruiz 2013). To obtain the last equality in Equation (22), we have adopted the typical value $n = 5/3$. For $\gamma = 5/3$ and $\beta = 1$, we have $B_{5/3} = 0.1618$ (see the appendix of Guillochon & Ramirez-Ruiz 2013). Equation (22) gives the expected total accreted stellar mass $\Delta M_* \simeq 0.322 (A_\gamma B_\gamma / 0.215) m_* M_\odot$ after the peak time of the light curve. For a circular accretion disk of typical $\eta = 0.1$, the total accreted mass gives a total radiation energy of $\Delta E = \eta \Delta M_* c^2 \simeq 5.76 \times 10^{52} \text{ erg } \eta_{-1} (A_\gamma B_\gamma / 0.215) m_*$, which only depends on the mass of the star in a full disruption and is independent of the BH mass. For a typical star of mass $M_* = 0.3 M_\odot$, the expected total radiation energy is $\Delta E \simeq 1.73 \times 10^{52} \text{ erg } \eta_{-1} (A_\gamma B_\gamma / 0.215)$.

For the elliptical accretion disk with the radiation efficiency given by Equation (9), Equation (22) gives the total energy of radiation

$$\Delta E \simeq \eta \Delta M_* c^2$$

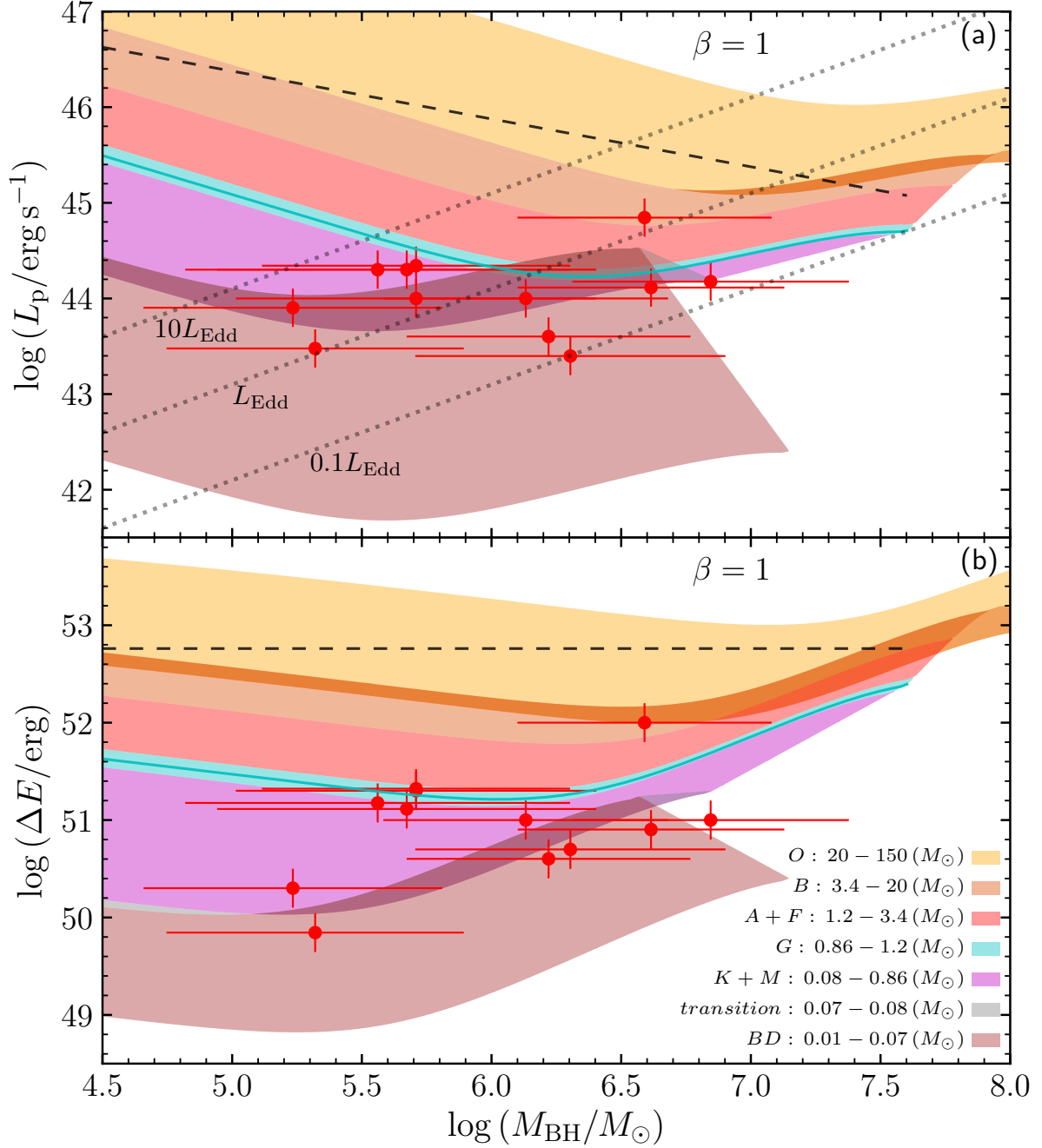


Figure 2. Peak luminosity (a) and total radiation energy after peak (b) vs. BH mass. The mass ranges of the stellar spectral types are adopted from Cox (2000) and are color-coded. The three dotted lines in panel (a) denote multiples of the Eddington luminosity. The dashed lines denote the peak luminosity L_{p} (panel a; Equation (20)) and the total radiation energy ΔE (panel b) for $M_{*} = 1 M_{\odot}$ and $\eta = 0.1$, while the solid lines in the cyan regions are for stellar mass $M_{*} = 1 M_{\odot}$ with the radiation efficiency η given by Equation (9). The shaded areas truncate at the BH mass where $r_{\text{t}} = r_{\text{ms}}$. The filled circles show the TDE sample sources with the BH mass calculated from the $M_{\text{BH}}-\sigma_{*}$ relation.

$$\begin{aligned}
 &\simeq \frac{\eta_0}{n-1} \left[2\delta + \sin^2 \left(\frac{\Omega}{2} \right) \right] A_\gamma B_\gamma m_* M_\odot c^2 \\
 &\simeq 1.36 \times 10^{51} \text{ erg} \left(\frac{\eta_0}{0.059} \right) \left(\frac{A_\gamma B_\gamma}{0.215} \right) \beta^{-1} m_*^{4/3} M_6^{-1/3} \times \\
 &\quad \left(1 + 0.25 \beta^3 r_*^{-2} m_*^{1/3} M_6^{5/3} \right), \tag{23}
 \end{aligned}$$

which depends not only on the mass of the star but also on the BH mass and orbital penetration factor of the star. For a solar-type star disrupted by a BH with a mass of $M_{\text{BH}} = 10^6 M_\odot$ and $10^7 M_\odot$, the total radiation energy is about 34 and 7 times lower, respectively, than that expected with the typical efficiency $\eta = 0.1$. Comparing the total energy radiated by circular versus eccentric disk models, we find that the missing energy problem (Piran et al. 2015) may be due to the high radiative efficiency of circular disk models. This problem is absent in the elliptical accretion disk model. We further discuss this point in Section 4. Figure 2(b) presents the expected total radiation energy as a function of M_{BH} and M_* for orbital penetration factor $\beta = 1$. We also show the expected total radiation energy computed for TDEs of solar-type stars with $\eta = 0.1$. Provided M_* , the expected total emitted energy weakly decreases with BH mass as $\Delta E \propto M_{\text{BH}}^{-1/3}$ until $M_{\text{BH}} \sim 2 \times 10^6 M_\odot \beta^{-9/5} r_*^{6/5} m_*^{-1/5} \sim 2 \times 10^6 M_\odot \beta^{-9/5} m_*^{1-1.2\zeta}$ and significantly increases when $M_{\text{BH}} \gtrsim 3 \times 10^6 M_\odot \beta^{-9/5} r_*^{6/5} m_*^{-1/5} \sim 3 \times 10^6 M_\odot \beta^{-9/5} m_*^{1-1.2\zeta}$. The transition occurs at $M_{\text{BH}} \sim 3 \times 10^6 M_\odot \beta^{-9/5} m_*^{1-1.2\zeta}$, with $\zeta = 0.21$ for $0.08 < m_* \leq 1$ and $\zeta = 0.44$ for $1 < m_* \leq 150$.

From the total radiation energy given in Equation (23), we can calculate the expected accreted stellar mass to power a TDE with the canonical radiation efficiency $\eta = 0.1$,

$$\begin{aligned}
 \Delta M_{\text{app}} &= \frac{\Delta E}{0.1 c^2} = \left(\frac{\eta}{0.1} \right) \Delta M_* \\
 &\simeq 15 \eta_0 \left[2\delta + \sin^2 \left(\frac{\Omega}{2} \right) \right] A_\gamma B_\gamma m_* M_\odot, \tag{24}
 \end{aligned}$$

which for $r_p \gg r_s$ gives

$$\begin{aligned}
 \Delta M_{\text{app}} &\simeq 7.61 \times 10^{-3} M_\odot \left(\frac{\eta_0}{0.059} \right) \left(\frac{A_\gamma B_\gamma}{0.215} \right) \beta^{-1} m_*^{4/3} M_6^{-1/3} \times \\
 &\quad \left(1 + 0.25 \beta^3 r_*^{-2} m_*^{1/3} M_6^{5/3} \right). \tag{25}
 \end{aligned}$$

Equations (24) and (25) show that the accreted stellar mass inferred with the canonical $\eta = 0.1$ is much lower than the actual accreted stellar mass given by Equation (22). This suggests that the observed low accreted stellar mass of TDEs is due to the high radiation efficiency adopted in the literature. In the following, we call the accreted stellar mass inferred with $\eta = 0.1$ in Equation (24) the apparent accreted stellar mass. The apparent accreted stellar mass after peak is $\Delta M_{\text{app}} \simeq 0.045 M_\odot$ (Equation 25) or $0.04 M_\odot$ (Equation 24) for $M_{\text{BH}} = 10^7 M_\odot$ and $M_* = 1 M_\odot$. The apparent accreted stellar mass is $\Delta M_{\text{app}} \simeq 3 \times 10^{-3} M_\odot$ and $7 \times 10^{-4} M_\odot$ for tidal disruptions of M stars with $M_* = 0.3 M_\odot$ and BDs with $0.03 M_\odot$ by a BH of mass $10^6 M_\odot$, respectively.

Both the peak luminosity and the total radiation energy depend on BH mass, star mass, and orbital penetration factor β . The fallback rate of full disruption weakly depends on β (Guillochon & Ramirez-Ruiz 2013; Stone et al. 2013; Ryu et al. 2020b), suggesting that the peak luminosity L_p and the total radiation energy ΔE depend on β mainly because of the radiation efficiency η . For a tidal disruption with $\Delta = 0.25 \beta^3 r_*^{-2} m_*^{1/3} M_6^{5/3} \lesssim 1$, or with $\beta \lesssim 2.1$ and $M_{\text{BH}} \lesssim 10^{6.5} M_\odot$, we have $L_p \propto \beta^{-1} (1 + \Delta) m_*^{(5+9\zeta)/6} M_6^{-5/6} \propto$

$\beta^{-1}(1+\Delta)m_*^{1.15}M_6^{-5/6}$, and the total radiation energy $\Delta E \propto \beta^{-1}(1+\Delta)m_*^{4/3}M_6^{-1/3}$ for $\zeta = 0.21$, both of which are nearly independent of the orbital penetration factor because $1.2 \lesssim \beta^{-1}(1+\Delta) \lesssim 1.6$ (which varies by only $\sim 30\%$) for $0.7 \lesssim \beta \lesssim 2.1$. Provided L_p and ΔE , we can uniquely determine the masses of the star and the BH, but we can only poorly constrain the penetration factor for TDEs of shallow orbital pericenter penetration $\beta \sim 1$, which is expected for most TDEs. By comparison, for tidal disruption with $\Delta \gg 1$ (either $\beta \gtrsim 2.5$, $m_* \lesssim 0.11$, or $M_{\text{BH}} \gtrsim 10^{6.7}M_\odot$), we have the peak luminosity $L_p \propto \beta^2 m_*^{(-5+21\zeta)/6} M_6^{5/6} \propto \beta^2 m_*^{-0.098} M_6^{5/6}$ and the total radiation energy $\Delta E \propto \beta^2 m_*^{(-1+6\zeta)/3} M_6^{4/3} \propto \beta^2 m_*^{0.087} M_6^{4/3}$, both strongly sensitive to the penetration factor and the BH mass, but nearly independent of the mass of the disrupted star. Given L_p and ΔE , we can uniquely determine the mass of BH and the orbital penetration factor, but not the mass of the star. The above analysis shows that the BH mass of TDEs can be well determined by observing L_p and ΔE . However, the mass of the disrupted star and the orbital penetration factor cannot be determined simultaneously: the mass of the disrupted star can be uniquely determined for TDEs with negligible relativistic apsidal precession of the most-bound stellar debris with $\Delta \lesssim 1$, or the penetration factor β can be well determined observationally if the relativistic apsidal precession of the most-bound stellar debris is significant with $\Delta \gg 1$.

4. COMPARISON WITH OBSERVATIONS

In Section 3 we calculated the expected peak luminosities and total radiation energies after the peak of TDEs within the framework of an elliptical accretion disk model. In this section, we compare the model predictions to the observations of the peak luminosities and total radiation energies of TDEs. We adopt a Λ CDM cosmology with $H_0 = 70 \text{ km s}^{-1} \text{ Mpc}^{-1}$, $\Omega_m = 0.3$, and $\Omega_\Lambda = 0.7$.

4.1. The observational data

Among the 30–60 TDEs and candidate TDEs¹ (Komossa 2015), some have well-observed peaks in their light curves and can be used in the comparison between the model prediction and observation. Because we are interested only in the energy released by the accretion disk formed from the tidal disruptions of stars, we include a TDE in the sample only when (1) it is not relativistically jetted, (2) the host galaxy does not show any long-term AGN activity, (3) the peak brightness is well detected, and (4) the location coincides with the nucleus of the host galaxy. The peak of the brightness is well detected if neither the observational time gap before nor after the maximum luminosity of the light curve is longer than 30 days in the rest frame of the source. We adopted 30 days as the upper limit of the observational time gap because the time between the disruption of a solar-type star by a BH of $M_{\text{BH}} = 10^6 M_\odot$ and the peak accretion rate is $\Delta t_p \simeq 59$ days. The fourth requirement ensures that the BH mass can be estimated from the empirical relation between BH mass and bulge stellar velocity dispersion ($M_{\text{BH}}-\sigma_*$ relation), if a measurement of σ_* is available. This latter requirement excluded from the final sample the TDE candidates ROTSE *Dougie* and AT 2018cow because they are off-nucleus, even though the peaks of the light curves have been well detected (Vinkó et al. 2015; Kuin et al. 2019; Margutti et al. 2019; Perley et al. 2019).

We assembled a final sample of 18 sources (Table 1). All except ASASSN-14li and SDSS J0952+2143 have well-observed light-curve peaks in the wave bands of discovery. The peak brightness of TDE ASASSN-14li cannot be constrained in the optical/UV wave band of discovery because the observational time gap before the first detection of the event on 11 November 2014 is 121 days in the observer frame or 118.6 days in the source frame (Holoien et al. 2016b), although the peak was well detected in the soft

¹ An *Open TDE Catalog* is available at <https://tde.space>

Table 1. The Sample

Name	z	Type	Ref.	σ_*	Ref.	$\log(M_{\text{BH},\sigma})$	$\log(M_{\text{tot}})$	Ref.	$\log(M_{\text{BH,tot}})$	B/T^a	L_p	Ref.	ΔE	Ref.
(1)	(2)	(3)	(4)	(km s ⁻¹)	(6)	(M_\odot)	(M_\odot)	(9)	(M_\odot)	(11)	(10 ⁴⁴ erg s ⁻¹)	(13)	(10 ⁵⁰ erg)	(15)
iPTF16fnl	0.0163	Opt./UV	1,2	55±2	3	5.32 ^{+0.57} _{-0.58}	9.8	4	5.61 ± 0.65	0.29	0.3	2	0.7 ^b	2
AT 2018dyb	0.0180	Opt./UV	5	96±1	5	6.62 ^{+0.51} _{-0.52}	10.08	5	6.06 ± 0.65	0.43	1.3	5	8 ^b	5
ASASSN-14li	0.0206	Opt./UV	6	78±2	3	6.13 ^{+0.55} _{-0.55}	9.6	4	5.29 ± 0.65	0.22	1	6,7	10 ^b	6,7
ASASSN-14ae	0.0436	Opt./UV	8	53±2	3	5.23 ^{+0.58} _{-0.58}	9.8	4	5.61 ± 0.65	0.29	0.8	8	2 ^b	8
ASASSN-15oi	0.0479	Opt./UV	9	61±7	10	5.56 ^{+0.74} _{-0.77}	9.9	4	5.77 ± 0.65	0.34	2	11	15 ^b	11
PTF09ge	0.064	Opt./UV	12	81±2	3	6.22 ^{+0.55} _{-0.55}	10.1	4	6.09 ± 0.65	0.44	0.4	13	4 ^b	13
iPTF15af	0.07897	Opt./UV	14	106±2	3	6.85 ^{+0.53} _{-0.53}	10.2	4	6.25 ± 0.65	0.47	1.5	14	10 ^b	14
SDSS J0952+2143	0.079	Opt./UV	15	95	15	6.59 ^{+0.49} _{-0.49}	10.37	16	6.53 ± 0.65	0.53	7	17	100 ^b	17
PS1-10jh	0.1696	Opt./UV	18	65±3	3	5.71 ^{+0.59} _{-0.60}	9.5	4	5.13 ± 0.65	0.19	2.2	18	21	18
PTF09djl	0.184	Opt./UV	12	64±7	3	5.67 ^{+0.73} _{-0.76}	10.1	4	6.09 ± 0.65	0.44	2	13	13 ^b	13
GALEX D23H-1	0.1855	Opt./UV	19	84±4	10	6.30 ^{+0.60} _{-0.60}	10.3	4	6.41 ± 0.65	0.51	0.25	19	5 ^b	19
GALEX D1-9	0.326	Opt./UV	20	65±6	10	5.71 ^{+0.70} _{-0.72}	10.3	4	6.41 ± 0.65	0.51	1	20	20 ^b	20
XMMSL1 J0740	0.0173	X-ray	21	~ 10.62 ^c	...	6.92 ± 0.65	0.60	2	21	6 ^b	21
ASASSN-19bt	0.0262	Opt./UV	22	10.04	22	6.00 ± 0.65	0.41	1.3	22	10 ^b	22
AT 2018fyk	0.059	Opt./UV	23	10.2	23	6.25 ± 0.65	0.47	3	23	30 ^b	23
PS18kh	0.071	Opt./UV	24, 25, 26	10.15	24	6.17 ± 0.65	0.46	0.9	24	7 ^b	24
AT 2017eqx	0.1089	Opt./UV	27	9.36	27	4.90 ± 0.65	0.14	1	27	4 ^b	27
PS1-11af	0.4046	Opt./UV	28	10.1	4	6.09 ± 0.65	0.44	0.8	28	6 ^b	28

NOTE—The sample sources are divided into two groups: the upper part of the table shows the sources with a measurement of the stellar velocity dispersion of the host galaxies, and the lower part shows the sources without such a measurement.

^a The bulge-to-total mass ratio (B/T) is estimated with an empirical relation between B/T and the total stellar mass of the galaxy (Stone et al. 2018). It is obtained by averaging the B/T for different total stellar mass bins and has a very large uncertainty.

^b The energy is obtained by extrapolating the observations from the period of observational campaign to infinity.

^c The total stellar mass is estimated with the the 2MASS apparent K -band magnitude $K = 10.96$ mag (Saxton et al. 2017) and the average stellar mass-to-light ratio (M/L) (Bell et al. 2003). This is only a rough estimate, as we lack the color of the host galaxy.

References—(1) Blagorodnova et al. (2017), (2) Brown et al. (2018), (3) Wevers et al. (2017), (4) van Velzen (2018), (5) Leloudas et al. (2019), (6) Holoien et al. (2016a), (7) Brown et al. (2017), (8) Holoien et al. (2014), (9) Holoien et al. (2016b), (10) Wevers et al. (2019b), (11) Holoien et al. (2018), (12) Arcavi et al. (2014), (13) van Velzen et al. (2019b), (14) Blagorodnova et al. (2019), (15) Komossa et al. (2008), (16) Graur et al. (2018), (17) Palaversa et al. (2016), (18) Gezari et al. (2012), (19) Gezari et al. (2009), (20) Gezari et al. (2008), (21) Saxton et al. (2017), (22) Holoien et al. (2019b), (23) Wevers et al. (2019a), (24) Holoien et al. (2019a), (25) van Velzen et al. (2019a), (26) Hung et al. (2019), (27) Nicholl et al. (2019), (28) Chornock et al. (2014)

X-rays (Miller et al. 2015; Brown et al. 2017; Bright et al. 2018). TDE candidate SDSS J0952+2143 was discovered through the detection of transient ultra-strong optical emission lines during the SDSS survey (Komossa et al. 2008) and has an unfiltered optical light curve from the Lincoln Near Earth Asteroid Research (LINEAR) survey (Palaversa et al. 2016). Table 1 divides the sample into two groups, according to whether or not stellar velocity dispersion is available for the host galaxy. Both luminosity-weighted and central line-of-sight velocity dispersions are measured in the literature, and there is no significant difference between them (Wevers et al. 2017, 2019b). The velocity dispersions are not affected significantly by the presence of disks in the host galaxies. Column 7 gives the BH mass obtained with the host stellar velocity dispersion in Column 5. Extensive works on the $M_{\text{BH}}-\sigma_*$ relation have been published in the literature and indicate that the $M_{\text{BH}}-\sigma_*$ relation depends both on the type of host galaxy and on the range of the BH masses in the sample (e.g., Kormendy & Ho 2013). Because TDEs are expected to occur in all types of galaxies, neither the $M_{\text{BH}}-\sigma_*$ relation obtained from the early-type galaxies nor the

one from the late-type galaxies could give good estimates of the BH masses of TDEs. Therefore, we estimate the BH masses using the $M_{\text{BH}}-\sigma_*$ relations obtained from all types of galaxies (van den Bosch 2016; She et al. 2017). Because the early- and late-type galaxies have their own $M_{\text{BH}}-\sigma_*$ relations with different slopes and zeropoints, the obtained $M_{\text{BH}}-\sigma_*$ relation depends on the sample of galaxies. With the tabulated data of all types of galaxies (Kormendy & Ho 2013), She et al. (2017) obtained the relation $\log(M_{\text{BH}}/M_{\odot}) = (8.32 \pm 0.05) + (5.20 \pm 0.37)\log(\sigma_*/200 \text{ km s}^{-1})$ with an intrinsic scatter of 0.44 dex. Because most TDEs are expected to be caused by a BH of mass lower than $10^8 M_{\odot}$, here we calculate the BH masses with the $M_{\text{BH}}-\sigma_*$ relation, $\log(M_{\text{BH}}/M_{\odot}) = (8.32 \pm 0.04) + (5.35 \pm 0.23)\log(\sigma_*/200 \text{ km s}^{-1})$ with the intrinsic scatter of 0.49 ± 0.03 dex (van den Bosch 2016), which are consistent with the results obtained by She et al. (2017; with the difference of $\Delta\log(M_{\text{BH}}/M_{\odot})$ ranging from 0.04 for $\sigma_* = 110 \text{ km s}^{-1}$ to 0.08 for $\sigma_* = 55 \text{ km s}^{-1}$; see Figure 10(b) for a detailed comparison). We note that the BH mass obtained in this way is from more low-mass objects and the sample is twice as large as the most previously studied sample. The uncertainties of the BH mass in Table 1 come from both the observational uncertainties of stellar velocity dispersion and the intrinsic scatter of the $M_{\text{BH}}-\sigma_*$ relation. Although TDEs are expected to occur in all types of galaxies, the spectroscopical observations show that the host galaxies of most known TDEs are E+A or post-starburst galaxies (Arcavi et al. 2014; French et al. 2016). Post-starburst galaxies are in transition between star-forming spirals and passive early-type galaxies. No $M_{\text{BH}}-\sigma_*$ relation specifically for post-starburst galaxies is available in the literature. We may estimate the BH masses of post-starburst galaxies by averaging the BH masses obtained separately with the $M_{\text{BH}}-\sigma_*$ relations for early- and late-type galaxies. Using this method and the relations in McConnell & Ma (2013), we obtain the interpolated $M_{\text{BH}}-\sigma_*$ relation for TDEs,

$$\log(M_{\text{BH}}/M_{\odot}) = 8.23 + 5.13 \log(\sigma_*/200 \text{ km s}^{-1}). \quad (26)$$

The last equation is nearly independent of the distributions of the BH masses in the subsample galaxies.

It has recently been suggested that the BH mass may correlate with the total stellar mass of the host galaxy (Reines & Volonteri 2015). The relation between the BH mass and the total galactic stellar mass obtained from the AGN sample has been used to estimate the BH masses of TDEs in the literature (e.g., Gezari et al. 2017; Lin et al. 2017b; Holoien et al. 2018; Leloudas et al. 2019; Saxton et al. 2019; Wevers et al. 2019b). The relation between the BH mass and the total galactic stellar mass has recently been updated (Greene et al. 2020). Columns 8 and 9 list the total stellar masses of the host galaxies and the references, and Column 10 is the BH mass estimated with the $M_{\text{BH}}-M_{\text{tot}}$ relation, $\log(M_{\text{BH}}/M_{\odot}) = 6.70 + 1.61 \log(M_{\text{tot}}/3 \times 10^{10} M_{\odot})$ (Greene et al. 2020). When more than one measurement of the total stellar mass is available in the literature, we adopted one of them in the calculations. For XMMSL1 J0740, no measurement of the total stellar mass is available in the literature. We use the 2MASS apparent K -band magnitude $K = 10.96$ (Saxton et al. 2017) and adopt the average mass-to-light ratio (M/L_K) as a function of total stellar mass from the appendix of Bell et al. (2003) to estimate the total stellar mass of the host of XMMSL1 J0740. Because the stellar mass-to-luminosity ratio M/L_K is color-based (although it is less sensitive in K band) and we lack the color information, the total stellar mass of the host galaxy is only a rough estimate. We note that the BH mass of XMMSL1 J0740, $M_{\text{BH}} \sim 10^{6.92} M_{\odot}$, estimated from the total stellar mass, is consistent with the results of Saxton et al. (2017)². Because it is difficult to compute the uncertainty of the total stellar mass of the host galaxy, the uncertainty of BH mass in Column 10 is only due to the scatter of the $M_{\text{BH}}-M_{\text{tot}}$ relation.

² The measurement of the host stellar mass of XMMSL J0740 could be $3-3.5 \times 10^9 M_{\odot}$ based on private communication with Saxton. The BH mass estimated with the measurement and the $M_{\text{BH}}-M_{\text{tot}}$ relation is about $10^5 M_{\odot}$, about two order of magnitude lower than the value quoted in the table and roughly consistent with the MCMC result in Table 3.

Column 11 gives the ratio (B/T) of the bulge and total stellar mass of the host galaxy. Because the bulges of the host galaxies of most TDEs are not resolved, we estimate B/T from the empirical relation between the mass ratio B/T and the total stellar mass of the galaxy (Stone et al. 2018). The correlation of the mass ratio B/T and the total stellar mass of the galaxy has a very large scatter. The total stellar masses of the sample galaxies in Stone et al. (2018) are binned, and the ratio B/T in Table 1 is the average of each bin, which, we note, has very large uncertainties.

Table 1 lists the peak bolometric luminosities. Ideally, the peak bolometric luminosity should be obtained by integrating the spectral energy distribution from the optical/UV to the X-rays at the time of peak brightness. However, in practice, we cannot observe in the extreme UV (EUV) because of Galactic extinction. Therefore, an extrapolation from a single or several wave bands to obtain bolometric luminosity is required. Different approaches have been followed in the literature. Some only measure the luminosity in the observed band without any further extrapolation. The emission of an accretion disk with an inner edge at the ISCO, as in AGNs or BH X-ray binaries, is broader than a single blackbody. As in AGNs, some authors apply a bolometric correction, which can be up to a factor of 10, to account for an unobservable EUV bump. However, an elliptical accretion disk is truncated at an inner edge much larger than the ISCO: $a_{\text{in}} \simeq r_{\text{ms}}/(1-e_{\text{d}}) \sim r_{\text{ms}}a_{\text{mb}}/[(1-e_{\text{mb}})a_{\text{mb}}] \sim [r_{\text{ms}}/r_{\text{ISCO}}][a_{\text{mb}}/r_{\text{p}}]r_{\text{ISCO}} \sim 50\beta m_*^{-1/3} M_6^{1/3} r_{\text{ISCO}}$. Hence, the disk emission in the EUV and soft X-ray wave bands is expected to be much less significant than that of a standard thin accretion disk. The observed spectral energy distributions of TDEs can be fit well by a single blackbody with a temperature of about 10^4 K, much lower than the prediction of a standard thin accretion disk with a typical temperature of $T \gtrsim 10^5$ K (e.g., Gezari et al. 2012; Holoien et al. 2014, 2016b; Brown et al. 2017). Therefore, many authors approximate the observed spectral energy distribution by a single blackbody and then determine the bolometric luminosity by integrating over this single blackbody. Our paper follows the latter method. We calculate the bolometric luminosity by integrating over a single blackbody for the optical and UV radiation and then add the contribution from the soft X-ray band at the time of peak brightness. The only exception is for the X-ray TDE XMMSL1 J0740, for which we use the bolometric luminosity from Saxton et al. (2017). The optical/UV fluxes are corrected for Galactic extinction and host galaxy starlight. No correction for internal extinction is made because there is no significant evidence of internal dust extinction reported for most TDEs. Based on the ratio of He II $\lambda 3203/\lambda 4686$, Gezari et al. (2012) suggest that internal extinction might be important for PS1-10jh, but the origin of the broad optical lines remains unclear, likely arising from an optically thick outflow envelope (Roth et al. 2016) or a highly eccentric, optically thick accretion disk (Liu et al. 2017). For GALEX D23H-1, significant extinction from the host galaxy can be deduced from the Balmer decrement, but the extinction along the line of sight to the flare may be different (Gezari et al. 2009). Except for the TDE candidate SDSS J0952+2143, we obtain optical luminosities for most optical/UV TDEs by integrating the blackbody fit to the spectral energy distributions, whose temperatures are obtained from multiwave band observations at the peak of the light curves. In the event that temperature at the peak is unavailable, we extrapolate it from observations after the peak assuming a constant temperature. For SDSS J0952+2143, only unfiltered observations are available at the time of peak brightness, and we approximate the optical-UV spectral energy distribution with a blackbody of temperature 3.5×10^4 K (Komossa et al. 2008).

When available, the X-ray luminosity at the peak brightness is included in the bolometric luminosity. However, except for ASASSN-14li (Brown et al. 2017), the X-ray radiation at peak brightness is either undetected or insignificant for most of the optical/UV TDEs. The optically selected TDE candidate GALEX D1-9 was detected in X-rays ~ 2.1 yr after the peak (Gezari et al. 2008), but its contribution at peak bright-

ness is unknown. Its behavior may be similar to that of other optical TDEs that were observed to be extremely weak in the X-rays at the time of the peak but subsequently became much stronger at late times (ASASSN-15oi: [Gezari et al. 2017](#); PTF09axc, PTF09ge, and ASASSN-14ae: [Jonker et al. 2020](#)). The peak bolometric luminosity of GALEX D1-9 (Table 1) is the integral of the blackbody fit to the optical/UV spectral energy distribution at the peak brightness. Because it is difficult to estimate the uncertainties of the peak bolometric luminosities, we assign to them an uncertainty of 0.2 dex ($\sim 60\%$).

We note that the total radiation energies after peak for some sources are integrated only up to the end of their observational campaign. To correct for this limitation, we calculate the total radiation energy ΔE by extrapolating the observations to infinite time with Equation (18), using

$$\Delta E = \frac{\Delta E_0}{1 - [L_e/L_p]^{1-1/n}} \quad (27)$$

with $n = 5/3$, where ΔE_0 is the radiation energy integrated from the peak time t_p to time t_0 of the end of the observational campaign and L_e is the luminosity at t_0 . Two objects required special treatment. For ASASSN-14ae, the bolometric luminosity is best fit with an exponential ([Holoien et al. 2014](#)), and for PS18kh, which rebrightened at ~ 50 days (rest frame) after the peak until 70 days after the peak when the observational campaign ended, we extrapolate the observations by assuming a power-law decay of the luminosity given by Equation (18) and taking t_d from [Holoien et al. \(2019a\)](#). It is difficult to estimate the uncertainty of the total radiation energy, but for simplicity, we assume it to be 0.2 dex.

4.2. Consistency between model predictions and observations

Figure 2 shows the observed peak bolometric luminosity and the total radiation energy as a function of the BH mass calculated from the $M_{\text{BH}}-\sigma_*$ relation. As explained in Section 4.1, we assume that L_p and ΔE gave uncertainties of 0.2 dex. Both the observed peak bolometric luminosity and the total radiation energy correlate tentatively with the BH mass, consistent with the results obtained by [Wevers et al. \(2017, 2019b\)](#). These results, in combination with the absence of a connection between blackbody temperature and BH mass ([Wevers et al. 2017, 2019b](#)), are at odds with the predictions of the shock-powered model of [Piran et al. \(2015\)](#) but are expected for the elliptical accretion disk model of roughly uniform eccentricity ([Liu et al. 2020](#)). Figure 2 shows that the observed peak bolometric luminosity and the total radiation energy are consistent with the expectations from the elliptical accretion disk model with orbital penetration factor $\beta = 1$, but much lower than those expected with the canonical radiation efficiency $\eta = 0.1$. The results suggest that the sample TDEs probably result from the tidal disruption of stars of type A or later by supermassive BHs of mass between $10^5 M_\odot$ and $10^7 M_\odot$. This is consistent with the observation that the host galaxies of most TDEs are post-starbursts, for which star formation occurred about a billion years ago, and hence presently have a deficit of B- and O- type stars but are rich in stars of type A and later ([Arcavi et al. 2014](#); [French et al. 2016](#); [Law-Smith et al. 2017](#); [Graur et al. 2018](#)). The sole exception is the star-forming galaxy SDSS J0952+2143 ([Palaversa et al. 2016](#)), whose TDE probably arose from a disrupted early A-type or late B-type star. To summarize: given L_p , ΔE , and M_{BH} , we can solve Equations (21) and (23) to obtain the mass M_* and orbital penetration factor β .

4.3. Mass of the star and the accreted fraction

With the observations of the BH mass M_{BH} , the peak bolometric luminosity L_p , and the total radiation energy after peak ΔE (or apparent accreted stellar mass ΔM_{app}), we can solve Equations (21) and (23)

(or (24)) to obtain the mass and orbital penetration factor of the star. We solve the equations using Markov Chain Monte Carlo (MCMC) with the python package emcee (Foreman-Mackey et al. 2013). The likelihood function is

$$-\frac{1}{2} \left[\frac{(\log L_p - \log L'_p)^2}{\sigma_L^2} + \ln(2\pi\sigma_L^2) + \frac{(\log \Delta E - \log \Delta E')^2}{\sigma_E^2} + \ln(2\pi\sigma_E^2) \right], \quad (28)$$

where L_p and ΔE are the observed peak bolometric luminosity and the total radiation energy after peak, respectively, and L'_p and $\Delta E'$ are the estimates of Equations (21) and (23), respectively, with the input parameters (M_{BH} , M_* , and β), σ_L of 0.2 dex is the uncertainty of the peak bolometric luminosity, and σ_E of 0.2 dex is the uncertainty of the total radiation energy after peak. The prior parameters of the MCMC experiments are the BH mass M_{BH} , the stellar mass M_* , and the orbital penetration factor β of star. The prior distribution of M_* and β are uniform in the ranges of $0.01 M_\odot < M_* < 150 M_\odot$ and $0.9 \leq \beta \leq 2.5$, respectively. By fitting the multiwavelength light curves of a sample of TDEs, Mockler et al. (2019) showed that most of the TDEs have $\beta \simeq 1$ with a range $0.9 \lesssim \beta \lesssim 1.8$. We adopted the lower limit $\beta_l = 0.9$ because the method would give a poor constraint on β and the survey of TDEs would prefer detecting the full tidal disruption of stars to the partial disruptions as the former would give rise to higher peak luminosity and longer duration of TDE flares. Although an upper limit $\beta_u = 2.5$ is small and numerical hydrodynamic simulations of tidal disruptions with larger penetration factor β have been carried out in the literature (Evans et al. 2015; Sądowski et al. 2016; Darbha et al. 2019), we adopt $\beta_u = 2.5$ in this work and expect that the results except for β are not changed significantly by increasing the upper limit of the penetration factor. The reason is as follows. The posterior distributions of β in Figure 3 (also in Figure 6 and Figure 7) show that β is not constrained well for the sample sources. Both the peak bolometric luminosity L_p and the total radiation energy after peak ΔE depend on the penetration factor β mostly because of the parameter Δ of the radiation efficiency η . Equations (21) and (23) show that for $\Delta \lesssim 1$, L_p and ΔE depend very weakly on β and their solutions would give poor constraints on the penetration factor. For $\Delta \gg 1$ (or $\beta \gg 1$) or $\Delta \ll 1$ (or $\beta \ll 1$), both L_p and ΔE change significantly with β . The penetration factor β can be well determined, and Equations (21) and (23) should be solved with the results of numerical hydrodynamic simulations with much larger ranges of penetration factor (Evans et al. 2015; Sądowski et al. 2016; Darbha et al. 2019). Because the 18 sample sources have $\Delta \lesssim 1$, the adopted range of penetration factor $0.9 \leq \beta \leq 2.5$ is reasonable, and the obtained penetration factors of the sample sources including those with $\beta \sim 2.5$ are rough estimates with large uncertainties. The prior distribution of the parameter M_{BH} is a normal distribution whose mean and variance corresponding to the observed values and their uncertainties, respectively, given in Column 7 of Table 1. The MCMC chain includes 100 walkers with each walker consisting of 10^4 steps. The first 50% of the steps of each walker are removed for burn-in and one set of the parameters is saved every five steps for the rest of the walkers. For each walker, the parameters begin with the local best-fit results from the least-squares method plus a small random offset.

Figure 3 shows the posterior distributions of model parameters (M_{BH} , M_* , and β) of the MCMC experiments, and Table 2 gives the results of the parameters M_* and β and the associated uncertainties at the 90% confidence level obtained with the MCMC method. Figure 3 shows that the BH and stellar masses of TDEs can be well determined, but the orbital penetration factor of the star is constrained poorly. These results are consistent with the arguments for TDEs with $\Delta = 0.25\beta^3 r_*^{-2} m_*^{1/3} M_6^{5/3} \lesssim 1$, or with $\beta \sim 1$ and $M_{\text{BH}} \lesssim 10^{6.5} M_\odot$ given at the end of Section 3. Our MCMC experiments show that some TDEs may have two solutions, one associated with a main-sequence star and the other associated with a BD. This is possible because the main-sequence stars and BDs have significantly different relations of stellar mass and radius,

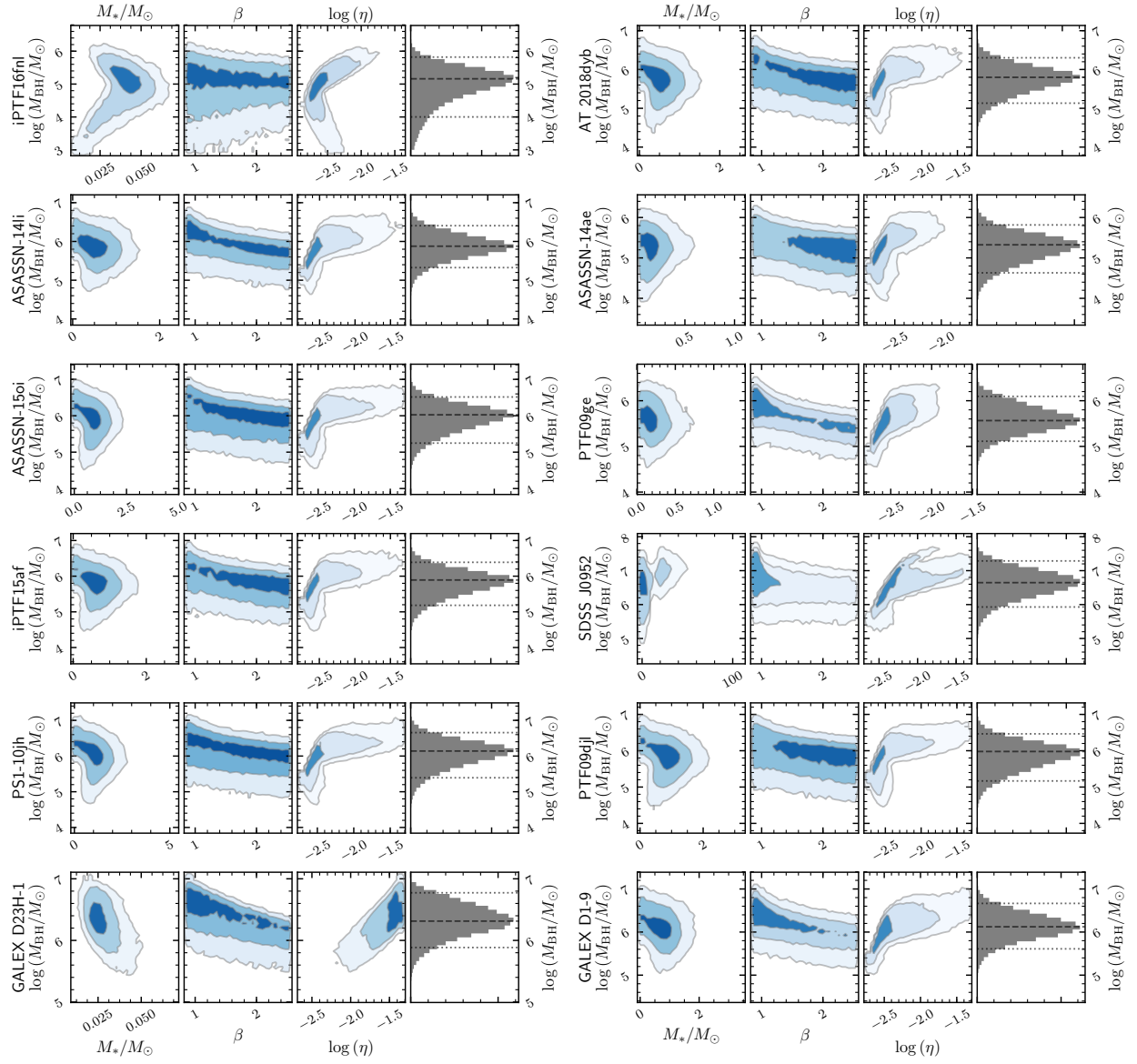


Figure 3. Posterior distributions of the model parameters (M_{BH} , M_* , and β) and the radiation efficiency (η). The contours are for 1, 2, and 3 σ . In the histogram of M_{BH} , the dashed line indicates the BH mass at the peak of the distribution, and the two dotted lines give the BH mass ranges at the 90% confidence level.

with a dramatic transition from $M_* \sim 0.07$ to $0.08 M_\odot$: The radius increases with mass for main-sequence stars but decreases with mass for a BD. We do not simply remove the solutions associated with BDs. We compare the probabilities of the posterior distributions of the two solutions and adopt the one with higher posterior probability to be the main solution of the TDE. Figure 3 gives the posterior distributions of the model parameters of the main solution. We give our conclusions based on the primary solutions of the TDEs. However, when the ratio of the probabilities associated with the two solutions is lower than 3 : 1, we keep both solutions and give the secondary solution in the row after the primary of Table 2.

Figure 4 shows the masses of the stars of the 12 TDEs obtained with the MCMC experiments, including both the primary and secondary possible solutions. Figure 4 and Table 2 show that the stars have spectral types ranging from A- through M-type main-sequence stars to BDs. Among all the 12 sample sources

with BH mass obtained with $M_{\text{BH}}-\sigma_*$ relations, iPTF16fnl and GALEX D23H-1 both have two solutions, with the primary solutions associated with a BD and the secondary associated with a main-sequence star. TDE iPTF16fnl has the lowest total radiation energy and the second lowest peak bolometric luminosity after GALEX D23H-1. It also has a light curve of the decay timescale that is among the shortest and has a BH among the lowest mass (Blagorodnova et al. 2017; Onori et al. 2019). Therefore, the main solution for iPTF16fnl associated with a BD is likely the real solution of the source. TDE GALEX D23H-1 has the lowest peak bolometric luminosity and is one of the sources with the lowest total radiation energy. These factors lead to the solution of a BD. However, the low peak bolometric luminosity and total radiation energy of GALEX D23H-1 might not be intrinsic but due to a possible intrinsic dust extinction of the host galaxy because a global extinction has been detected with the Balmer decrement of the H II regions and the extinction in the line of sight to the flare might be important (Gezari et al. 2009). Except for iPTF16fnl and GALEX D23H-1, the other 10 sample sources with observations of a BH mass have solutions associated with late-type main-sequence or A-type stars. Our result that most stars of the TDE sources are late-type main-sequence stars or BDs is well consistent with the fact that the host galaxies of most TDEs except for SDSS J0952+2143 are post-merger E+A galaxies, with the last burst occurring about a billion years ago, so that the stellar population in the centers are dominated by stellar types A and later (Arcavi et al. 2014; French et al. 2016, 2017).

When we calculated the peak bolometric luminosity with $L_p = \eta \dot{M}_p c^2$ and the total radiation energy $\Delta E = \eta \Delta M_* c^2$ with the radiation efficiency η given by Equation (9), we have implicitly assumed that the peak bolometric luminosity is sub-Eddington. However, when the peak fallback rate \dot{M}_p is near or above the Eddington accretion rate $\dot{M}_{\text{Edd}} = L_{\text{Edd}}/(\eta c^2)$, the peak luminosity L_p scales as (Paczynski 1980) $L_p \simeq L_{\text{Edd}} [1 + \log(\dot{M}_p/\dot{M}_{\text{Edd}})]$ because of the photon trapping and because a significant fraction of radiation is advected onto the BH (Abramowicz et al. 1988). For TDEs with $\dot{M}_p \gtrsim \dot{M}_{\text{Edd}}$, the light curves are capped at the Eddington luminosity. To compare the observations of TDEs with the predictions of the elliptical accretion disk model, we excluded from the sample TDE sources the candidates with an extended plateau in their light curves (most of these TDE candidates are in AGNs). Meanwhile, transient surveys are more likely to detect bright TDEs. They preferentially detect TDEs with a peak luminosity at or near the Eddington luminosity. Therefore, if we assume $L_p \sim L_{\text{Edd}}$, Equation (21) gives

$$\begin{aligned} m_* &\simeq \left(\frac{1.25}{1.78}\right)^{6/(5+9\zeta)} \left[\left(\frac{\eta_0}{0.059}\right)^{-1} \left(\frac{A_\gamma}{1.328}\right)^{-1} \beta (1+\Delta)^{-1} \right]^{6/(5+9\zeta)} \left(\frac{L_p}{L_{\text{Edd}}}\right)^{6/(5+9\zeta)} M_6^{11/(5+9\zeta)} \\ &\simeq 0.70^{6/(5+9\zeta)} \left(\frac{L_p}{L_{\text{Edd}}}\right)^{6/(5+9\zeta)} M_6^{11/(5+9\zeta)}. \end{aligned} \quad (29)$$

For $\zeta \simeq 0.21$, we have

$$m_* \simeq 0.70^{6/6.89} \left(\frac{L_p}{L_{\text{Edd}}}\right)^{6/6.89} M_6^{11/6.89}. \quad (30)$$

Figure 4 also shows the selection effect according to Equation (30) for $L_p = L_{\text{Edd}}$ and $L_p = 0.1L_{\text{Edd}}$. Taking into account the large intrinsic scatter of the $M_{\text{BH}}-\sigma_*$ relation ($\sigma = 0.49$ dex or $3\sigma = 1.47$ dex), Figure 4 shows that the mass of the star may correlate with the mass of BH, which is consistent with the suggestion of Equation (30).

Given M_{BH} , M_* , and β , we can calculate the radiation efficiency, $\eta = \eta(M_{\text{BH}}, R_*, M_*, \beta)$, with Equation (9) and the MCMC method. The posterior distributions of η are given in Figure 3, and the radiation efficiencies

Table 2. Results of the MCMC experiments for the TDEs with BH mass provided

Name	M_* (M_\odot)	β	$\log(\eta)$	ΔM_* (M_\odot)	$\Delta M_*/M_*$
(1)	(2)	(3)	(4)	(5)	(6)
iPTF16fnl ^a	0.040 ^{+0.015} _{-0.017} 0.081 ^{+0.054} _{-0.008}	0.9 ^{+1.4} _{-0.0} 2.5 ^{+0.0} _{-1.3}	-2.68 ^{+0.45} _{-0.12} -2.74 ^{+0.18} _{-0.04}	0.012 ^{+0.005} _{-0.005} 0.026 ^{+0.011} _{-0.008}	0.34 ^{+0.00} _{-0.09} 0.34 ^{+0.00} _{-0.10}
AT 2018dyb	0.46 ^{+0.47} _{-0.38}	2.5 ^{+0.0} _{-1.4}	-2.64 ^{+0.53} _{-0.08}	0.13 ^{+0.13} _{-0.11}	0.34 ^{+0.00} _{-0.09}
ASASSN-14li	0.46 ^{+0.49} _{-0.38}	0.9 ^{+1.4} _{-0.0}	-2.57 ^{+0.54} _{-0.14}	0.15 ^{+0.13} _{-0.13}	0.34 ^{+0.00} _{-0.09}
ASASSN-14ae	0.14 ^{+0.17} _{-0.07}	2.5 ^{+0.0} _{-1.4}	-2.69 ^{+0.30} _{-0.06}	0.043 ^{+0.047} _{-0.022}	0.34 ^{+0.00} _{-0.09}
ASASSN-15oi	0.88 ^{+0.56} _{-0.79}	0.9 ^{+1.4} _{-0.0}	-2.61 ^{+0.65} _{-0.09}	0.25 ^{+0.17} _{-0.23}	0.34 ^{+0.00} _{-0.09}
PTF09ge	0.16 ^{+0.21} _{-0.08}	0.9 ^{+1.4} _{-0.0}	-2.59 ^{+0.35} _{-0.14}	0.050 ^{+0.060} _{-0.028}	0.34 ^{+0.00} _{-0.09}
iPTF15af	0.66 ^{+0.42} _{-0.57}	2.4 ^{+0.0} _{-1.4}	-2.62 ^{+0.56} _{-0.08}	0.17 ^{+0.14} _{-0.15}	0.34 ^{+0.00} _{-0.09}
SDSS J0952+2143	3.03 ^{+21.55} _{-2.35}	0.9 ^{+1.3} _{-0.0}	-2.30 ^{+0.53} _{-0.28}	0.98 ^{+0.71} _{-0.76}	0.31 ^{+0.01} _{-0.28}
PS1-10jh	1.02 ^{+0.69} _{-0.89}	0.9 ^{+1.4} _{-0.0}	-2.55 ^{+0.68} _{-0.13}	0.32 ^{+0.18} _{-0.29}	0.34 ^{+0.00} _{-0.09}
PTF09djl	0.83 ^{+0.53} _{-0.74}	2.4 ^{+0.1} _{-1.4}	-2.61 ^{+0.58} _{-0.10}	0.24 ^{+0.15} _{-0.21}	0.34 ^{+0.00} _{-0.09}
GALEX D23H-1 ^a	0.025 ^{+0.012} _{-0.007} 0.13 ^{+0.21} _{-0.05}	0.9 ^{+1.4} _{-0.0} 0.9 ^{+1.3} _{-0.0}	-1.40 ^{+0.04} _{-0.41} -2.57 ^{+0.37} _{-0.13}	0.0075 ^{+0.0039} _{-0.0025} 0.042 ^{+0.059} _{-0.020}	0.34 ^{+0.00} _{-0.09} 0.34 ^{+0.00} _{-0.08}
GALEX D1-9	0.74 ^{+0.44} _{-0.66}	0.9 ^{+1.4} _{-0.0}	-2.54 ^{+0.68} _{-0.14}	0.23 ^{+0.13} _{-0.20}	0.34 ^{+0.00} _{-0.09}

NOTE—The BH masses are calculated with the $M_{\text{BH}}-\sigma_*$ relation. The uncertainties of the model parameters are at the 90% confidence level obtained with MCMC experiments.

^aThe source has two possible solutions, and the main one with the higher probability is given at the first entry.

and the associated uncertainties at the 90% confidence level are given in Table 2. These results are also shown in Figure 1, where the BH masses are computed from the $M_{\text{BH}}-\sigma_*$ relation. Figure 1 shows that the radiation efficiencies are much lower than the canonical value $\eta = 0.1$ that is commonly adopted in the literature. All the TDE sources except GALEX D23H-1 have a typical radiation efficiency $\log(\eta) \simeq -2.57$ or $\eta \simeq 2.7 \times 10^{-3}$, which is about 37 times lower than the canonical radiation efficiency. A low radiation efficiency would lead to a low peak bolometric luminosity and a low total radiation energy for a given accretion rate of matter. In other words, given the observed peak bolometric luminosity and the total radiation energy after peak, we would obtain a much higher apparent accretion rate and total accreted stellar material due to the low radiation efficiency. Our result suggests that the low bolometric peak luminosity and total radiation energy of TDEs result from the low conversion efficiency of matter into radiation associated with the elliptical accretion disk.

Table 2 and Figure 5 give the masses of the accreted material ΔM_* and the fractions with respect to the masses of the disrupted stars (i.e., the accreted fraction of stellar mass) $\Delta M_*/M_*$ derived from the MCMC experiments. The accreted stellar mass together with the conversion efficiency gives the expected total radiation energy $\Delta E' = \eta \Delta M_* c^2$ of Equation (28). In Table 2 and Figure 5, we also give the associated

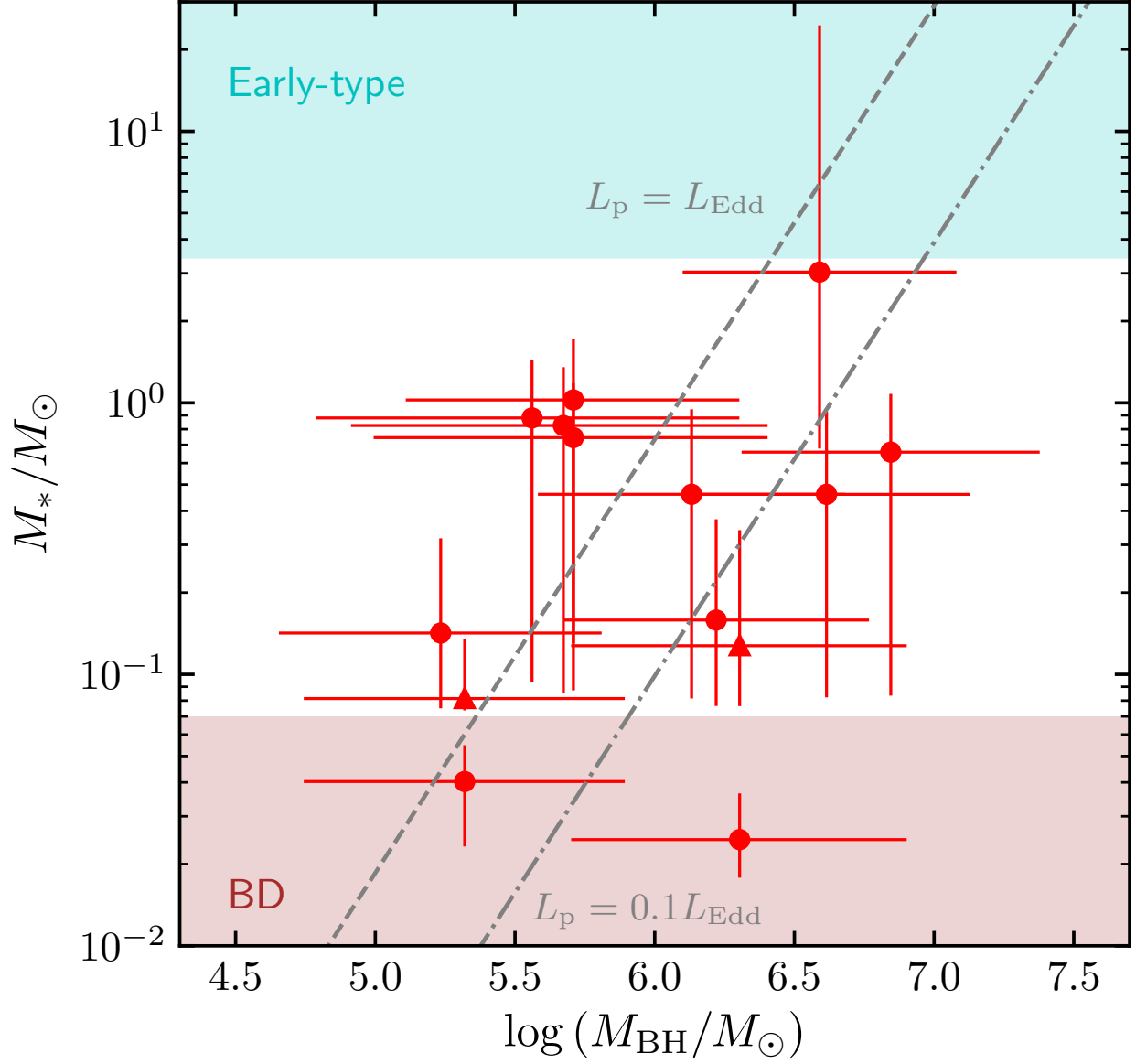


Figure 4. The stellar mass M_* (filled circles) vs. BH mass. The two color-shaded regions are for early-type stars (Early-type) and brown-dwarfs (BD). The filled triangles are for the secondary solutions of iPTF16fnl and GALEXD23H-1. The stellar mass and the associated uncertainty at 90% confidence level are calculated with the MCMC method. The dashed and dash-dotted lines refer to the observational selection effect according to Equation (30) for $L_p = L_{\text{Edd}}$ and $0.1 L_{\text{Edd}}$, respectively (see Section 4.3 for details).

uncertainties of ΔM_* and $\Delta M_*/M_*$ at the 90% confidence level. Equation (22) shows that the relative accreted stellar mass can be obtained with $\Delta M_*/M_* \simeq (1-n)^{-1} A_\gamma B_\gamma \simeq 1.5 A_\gamma B_\gamma$, which depends on the stellar structure and orbital penetration factor β (Lodato et al. 2009; Guillochon & Ramirez-Ruiz 2013; Golightly et al. 2019; Law-Smith et al. 2019; Ryu et al. 2020b). Therefore, in Figure 5, we also show the $\Delta M_*/M_*$ calculated with the empirical formulae of A_γ and B_γ in the appendix of Guillochon & Ramirez-Ruiz (2013) for both $\gamma = 5/3$ and $4/3$, while fixing $\beta = 1$. It shows that the total accreted material after peak significantly varies from about $10^{-2} M_\odot$ of GALEX D23H-1 and iPTF16fnl to about $1 M_\odot$ of SDSS J0952+2143, but the accreted material relative to the total mass of star of our TDEs except SDSS J0952+2143 is approximately

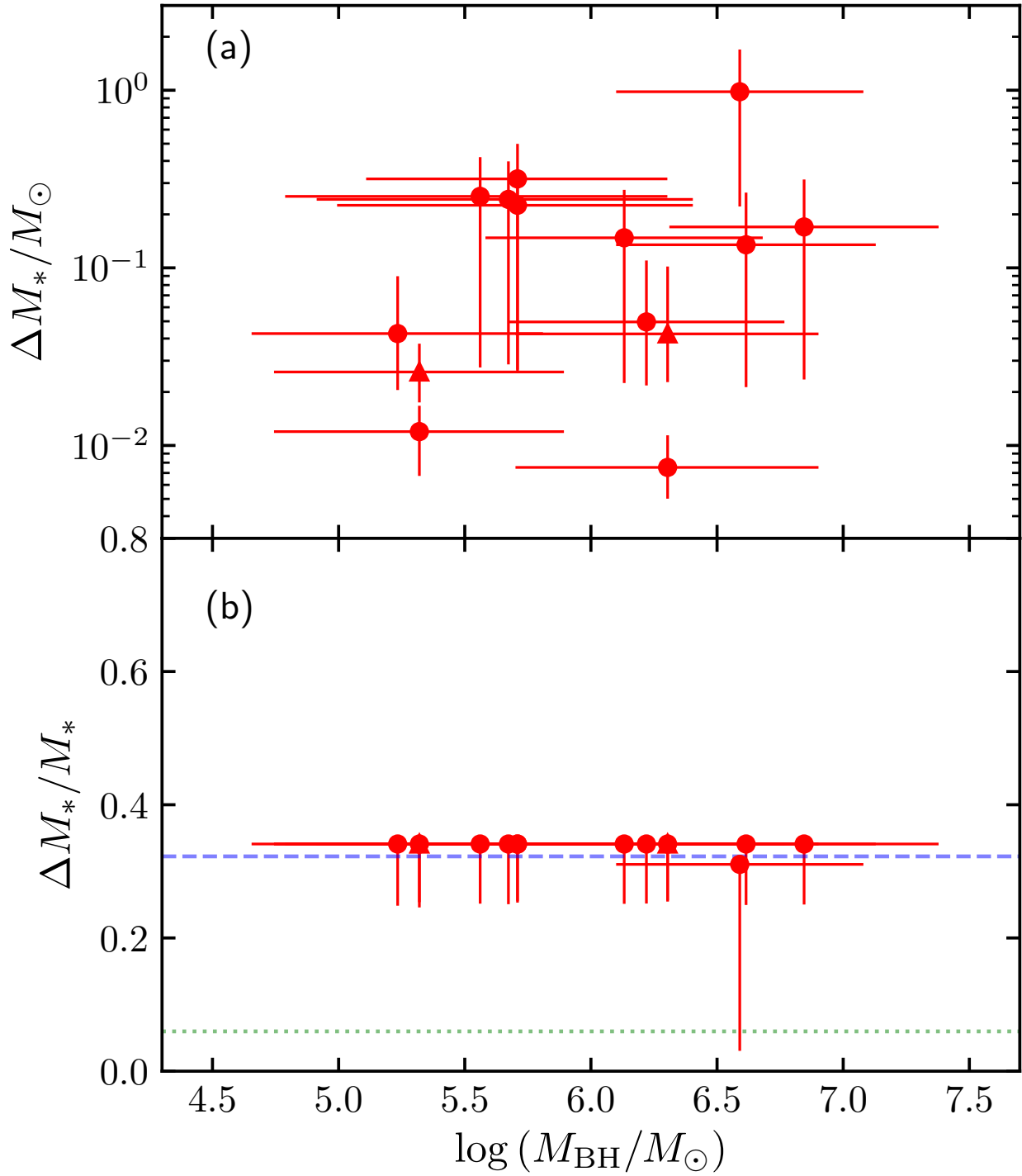


Figure 5. Accreted stellar mass after peak (a) and the relative accreted fraction (b) vs. BH mass for the sample sources in Table 2. The dashed and dotted lines in panel (b) show the prediction of the polytropic model assuming $\gamma = 5/3$ for low-mass stars and $\gamma = 4/3$ for high-mass stars, respectively. In both cases, $\beta = 1$ is assumed. The result of SDSS J0952+2143 with $M_* \simeq 3M_{\odot}$ is obtained with the hybrid polytropic model and close to the predictions with $\gamma = 5/3$.

constant, with $\Delta M_*/M_* \sim 0.34$, which is given by the hydrodynamic simulations of the tidal disruption of low-mass star with polytropic index $\gamma = 5/3$. For SDSS J0952+2143, the star has a mass of about $3.03 M_\odot$ and is described with our hybrid model. The relative accreted stellar mass of SDSS J0952+2143 is close to the expectation of the polytropic model $\gamma = 5/3$, but with very large uncertainties.

5. WEIGHING BHS USING TDES

5.1. Deriving the BH and stellar masses with L_p and ΔE

Since a massive BH could be a member of a supermassive BH binary, might lie in a globular cluster, or have an off-nuclear position, it is important to have an alternative method other than the $M_{\text{BH}}-\sigma_*$ relation to calculate the mass of the BH. Equations (19) and (22) show that provided the peak accretion rate \dot{M}_p and the total accreted material ΔM_* , one could uniquely determine the masses of the BH and the star by solving these two equations. However, we cannot directly measure \dot{M}_p and ΔM_* but the peak bolometric luminosity L_p and the total radiation energy ΔE , which depend not only on the masses of the BH and the star, but also on the radiation efficiency, the latter of which depends on the orbital penetration factor β . The solutions of the stellar mass and the BH mass become functions of the penetration factor and would be expected to be determined observationally with larger uncertainties. Figure 3 shows that even though we have the measurement of BH mass with the $M_{\text{BH}}-\sigma_*$ relation, the uncertainty in β is as large as the entire range of the prior. The large uncertainty is consistent with the arguments in Section 3 that the peak luminosity and the total radiation energy are nearly independent of the penetration factor for the range $0.7 \lesssim \beta \lesssim 2.1$ and implies that the mass of the BHs do not significantly couple with the penetration factor. We expect to determine the masses of the BHs and the stars with small uncertainties by solving Equations (21) and (23) given the observed L_p and ΔE . The uncertainty in β should not result in a large uncertainty in the measurement of the masses of the BHs and the stars.

With the observations of L_p and ΔE , we solve the equations with the MCMC method as described in Section 4.3, except that the prior distributions of all the three parameters M_{BH} , M_* and β are now uniform in the ranges $10^3 M_\odot \leq M_{\text{BH}} \leq 10^9 M_\odot$, $0.01 M_\odot < M_* < 150 M_\odot$, and $0.9 \leq \beta \leq 2.5$. The large ranges for the masses of BHs and stars require a large amount of computational time. To enhance the convergence rate of the MCMC experiments, we start the experiments with $\beta = 1$, and with the masses of the BH and the star that are calculated from Equations (21) and (23) and the observed L_p and ΔE for $\beta = 1$. We use these initial conditions because TDEs are expected to predominantly occur at $\beta \sim 1$ (Kochanek 2016; Stone & Metzger 2016). Since the results of the masses of the BH and the star depend only weakly on the penetration factor, the solutions obtained with $\beta = 1$ are good approximations.

We solve the equations for all the TDEs in Table 1 and give the posterior distributions of the model parameters ($\log M_{\text{BH}}$, M_* , and β) in Figure 6 and Figure 7 for the TDEs with and without the observations of the stellar velocity dispersion, respectively. In Figure 6 and Figure 7, we also give the posterior distributions of the associated radiation efficiency $\log \eta$ of the MCMC experiments. When a TDE has two possible solutions with comparable posterior probabilities, we give the posterior distribution of the primary solution in Figure 6. Table 3 shows the resulting masses of the BHs and stars, the radiation efficiency, and the associated uncertainties at the 90% confidence level. The posterior distributions of the model parameters (M_{BH} , M_* , β , and η) shown in Figure 6 are similar to those in Figure 3, implying that L_p and ΔE together can determine the mass of the disrupted star, the penetration factor, and the radiation efficiency as well as those when providing the BH masses. In Figure 8 we compare the masses of the disrupted stars derived with and without the knowledge of the BH masses. In the former case, the BH masses are given by the $M_{\text{BH}}-\sigma_*$

Table 3. Results of the MCMC experiments for all the sample sources

Name	$\log(M_{\text{BH}})$ (M_{\odot})	M_* (M_{\odot})	β	$\log(\eta)$	ΔM_* (M_{\odot})	$\Delta M_*/M_*$
(1)	(2)	(3)	(4)	(5)	(6)	(7)
iPTF16fnl ^a	5.16 ^{+0.66} _{-1.16}	0.040 ^{+0.015} _{-0.017}	0.9 ^{+1.4} _{-0.0}	-2.68 ^{+0.43} _{-0.13}	0.012 ^{+0.005} _{-0.005}	0.34 ^{+0.00} _{-0.09}
	4.96 ^{+0.51} _{-0.45}	0.082 ^{+0.055} _{-0.008}	2.5 ^{+0.0} _{-1.3}	-2.73 ^{+0.17} _{-0.05}	0.025 ^{+0.013} _{-0.007}	0.34 ^{+0.00} _{-0.10}
AT 2018dyb	5.80 ^{+0.50} _{-0.67}	0.46 ^{+0.48} _{-0.38}	2.5 ^{+0.0} _{-1.4}	-2.63 ^{+0.52} _{-0.09}	0.14 ^{+0.13} _{-0.12}	0.34 ^{+0.00} _{-0.09}
ASASSN-14li	5.88 ^{+0.53} _{-0.55}	0.41 ^{+0.53} _{-0.33}	0.9 ^{+1.4} _{-0.0}	-2.56 ^{+0.53} _{-0.14}	0.14 ^{+0.13} _{-0.12}	0.34 ^{+0.00} _{-0.09}
ASASSN-14ae	5.32 ^{+0.49} _{-0.69}	0.14 ^{+0.18} _{-0.06}	2.5 ^{+0.0} _{-1.4}	-2.69 ^{+0.31} _{-0.06}	0.043 ^{+0.047} _{-0.022}	0.34 ^{+0.00} _{-0.09}
ASASSN-15oi	6.03 ^{+0.49} _{-0.78}	0.89 ^{+0.53} _{-0.81}	2.3 ^{+0.1} _{-1.3}	-2.59 ^{+0.63} _{-0.10}	0.26 ^{+0.16} _{-0.23}	0.34 ^{+0.00} _{-0.09}
PTF09ge	5.57 ^{+0.53} _{-0.45}	0.15 ^{+0.22} _{-0.07}	0.9 ^{+1.4} _{-0.0}	-2.59 ^{+0.35} _{-0.14}	0.048 ^{+0.060} _{-0.026}	0.34 ^{+0.00} _{-0.09}
iPTF15af	5.89 ^{+0.50} _{-0.71}	0.57 ^{+0.51} _{-0.48}	2.5 ^{+0.0} _{-1.4}	-2.62 ^{+0.57} _{-0.08}	0.17 ^{+0.15} _{-0.14}	0.34 ^{+0.00} _{-0.09}
SDSS J0952+2143	6.65 ^{+0.64} _{-0.72}	2.99 ^{+21.11} _{-2.35}	0.9 ^{+1.3} _{-0.0}	-2.31 ^{+0.54} _{-0.27}	0.97 ^{+0.72} _{-0.75}	0.31 ^{+0.01} _{-0.28}
PS1-10jh	6.14 ^{+0.52} _{-0.75}	1.05 ^{+0.64} _{-0.95}	0.9 ^{+1.4} _{-0.0}	-2.57 ^{+0.70} _{-0.12}	0.30 ^{+0.20} _{-0.27}	0.34 ^{+0.00} _{-0.09}
PTF09djl	5.98 ^{+0.49} _{-0.81}	0.80 ^{+0.55} _{-0.71}	2.3 ^{+0.1} _{-1.3}	-2.61 ^{+0.61} _{-0.09}	0.24 ^{+0.16} _{-0.21}	0.34 ^{+0.00} _{-0.09}
GALEX D23H-1 ^a	6.31 ^{+0.46} _{-0.43}	0.025 ^{+0.012} _{-0.007}	0.9 ^{+1.4} _{-0.0}	-1.40 ^{+0.03} _{-0.43}	0.0074 ^{+0.0040} _{-0.0023}	0.34 ^{+0.00} _{-0.09}
	5.64 ^{+0.55} _{-0.40}	0.12 ^{+0.22} _{-0.05}	0.9 ^{+1.3} _{-0.0}	-2.58 ^{+0.38} _{-0.13}	0.047 ^{+0.057} _{-0.024}	0.34 ^{+0.00} _{-0.08}
GALEX D1-9	6.12 ^{+0.54} _{-0.51}	0.71 ^{+0.47} _{-0.63}	0.9 ^{+1.4} _{-0.0}	-2.54 ^{+0.69} _{-0.14}	0.20 ^{+0.15} _{-0.18}	0.34 ^{+0.00} _{-0.09}
XMMSL1 J0740	5.63 ^{+0.52} _{-0.91}	0.42 ^{+0.52} _{-0.32}	2.5 ^{+0.0} _{-1.4}	-2.65 ^{+0.34} _{-0.07}	0.13 ^{+0.14} _{-0.09}	0.34 ^{+0.00} _{-0.09}
ASASSN-19bt	5.88 ^{+0.52} _{-0.65}	0.53 ^{+0.51} _{-0.44}	0.9 ^{+1.4} _{-0.0}	-2.59 ^{+0.54} _{-0.12}	0.16 ^{+0.14} _{-0.14}	0.34 ^{+0.00} _{-0.09}
AT 2018fyk	6.27 ^{+0.52} _{-0.79}	1.39 ^{+0.88} _{-1.24}	0.9 ^{+1.4} _{-0.0}	-2.53 ^{+0.72} _{-0.13}	0.41 ^{+0.27} _{-0.36}	0.34 ^{+0.00} _{-0.09}
PS18kh	5.82 ^{+0.46} _{-0.63}	0.35 ^{+0.41} _{-0.27}	0.9 ^{+1.4} _{-0.0}	-2.64 ^{+0.53} _{-0.08}	0.11 ^{+0.11} _{-0.09}	0.34 ^{+0.00} _{-0.09}
AT 2017eqx	5.56 ^{+0.51} _{-0.66}	0.25 ^{+0.31} _{-0.18}	2.5 ^{+0.0} _{-1.4}	-2.67 ^{+0.43} _{-0.06}	0.079 ^{+0.081} _{-0.058}	0.34 ^{+0.00} _{-0.09}
PS1-11af	5.71 ^{+0.52} _{-0.55}	0.28 ^{+0.37} _{-0.20}	0.9 ^{+1.4} _{-0.0}	-2.58 ^{+0.44} _{-0.14}	0.091 ^{+0.097} _{-0.069}	0.34 ^{+0.00} _{-0.09}

^aThe source has two possible solutions, and the main one is given in the first entry.

NOTE—Results of the MCMC experiments are obtained with no prior knowledge of BH masses. A uniform prior distribution is adopted for the model parameters, including the BH masses. The uncertainties of the model parameters are determined by the 90% confidence level obtained with the MCMC experiments.

relation. It shows that the stellar masses derived in the above two cases are consistent with each other. This result suggests that the stellar mass and the amount of the accreted matter can be well constrained by L_p and ΔE . Figure 9 gives the stellar masses obtained with L_p and ΔE . It shows that the distributions of the stellar types of the TDEs with and without the observations of the stellar velocity dispersion are consistent. The stars of the TDE sample sources except iPTF16fnl and GALEX D23H-1 are A- or later-type main-sequence stars, which is consistent with the conclusions obtained by the TDEs with the observed stellar velocity dispersions. Figure 9 shows that the X-ray TDE XMMSL1 J0740 has the highest stellar mass for a given BH mass. However, the difference is not significant, and TDE XMMSL1 J0740 is the only sample source discovered in the X-ray wave band. Many more X-ray-discovered TDEs are needed. The

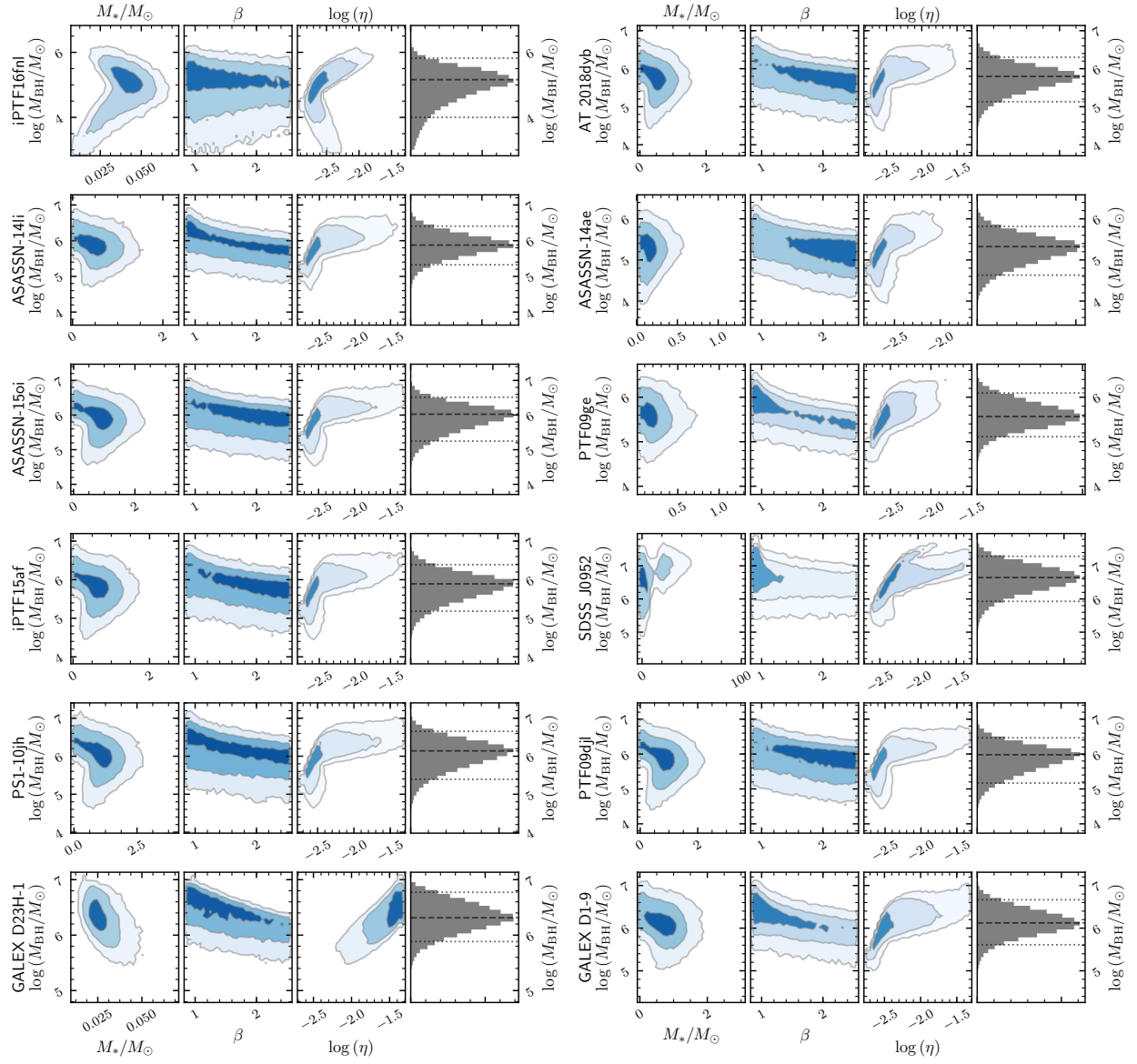


Figure 6. Posterior distributions of the model parameters and the radiation efficiency of the MCMC experiments. The results are for the TDE sources with observations of stellar velocity dispersion. A uniform prior distribution is adopted for all the model parameters (M_{BH} , M_* and β). Contour plots are for 1, 2, and 3 σ . The dashed and dotted lines are the same as in Figure 3. The main solution is shown when two solutions exist for a TDE.

correlation between the stellar and BH masses may be due to observational selection effects, as suggested by Equation (30).

In Figure 10(a) we compare the BH masses in Table 3 obtained with L_p and ΔE with those in Table 1 calculated with the $M_{\text{BH}}-\sigma_*$ relation. The one-to-one line and the intrinsic scatter of the $M_{\text{BH}}-\sigma_*$ relation are given to show the expected correlation and intrinsic scatter of the BH masses obtained from the two different methods. The uncertainty of the BH mass calculated with the $M_{\text{BH}}-\sigma_*$ relation includes both the observational uncertainty of the velocity dispersion and the intrinsic scatter of the $M_{\text{BH}}-\sigma_*$ relation. Figure 10(a) shows that the BH masses obtained with L_p and ΔE for all the TDEs except iPTF15af are consistent within one sigma with the BH masses obtained from the $M_{\text{BH}}-\sigma_*$ relation. The BH mass of

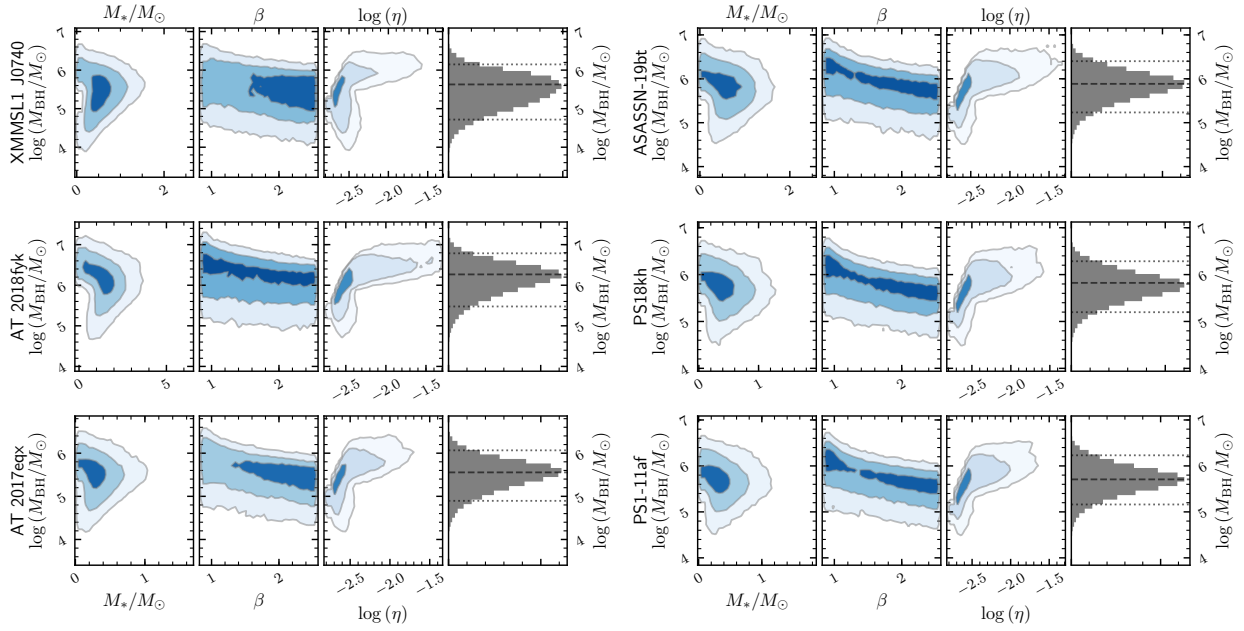


Figure 7. Same as in Figure 6, but for the TDE sources lacking stellar velocity dispersion measurements.

iPTF15af computed from L_p and ΔE is lower by 0.97 dex or 1.8 times the standard deviation (0.53 dex) than the mass obtained with the $M_{\text{BH}}-\sigma_*$ relation. The UV spectra of TDE iPTF15af have broad absorption lines associated with high-ionization states of N V, C IV, Si IV, and possibly P V. These features require an absorber with column densities $N_{\text{H}} > 10^{23} \text{ cm}^{-2}$ (Blagorodnova et al. 2019). Such an optically thick gas could significantly absorb the soft X-rays, if present. However, the observations of soft X-rays in the optically discovered TDEs suggested that the radiation in soft X-rays is much lower than or at most comparable to that in the optical and UV wave bands. Therefore, the low value of the BH mass of iPTF15af obtained with L_p and ΔE may not mainly be due to the absorption of soft X-rays, but to the intrinsic scatter of the $M_{\text{BH}}-\sigma_*$ relation. In Figure 10(b) we overplot the BH masses of the TDEs obtained with L_p and ΔE on the $M_{\text{BH}}-\sigma_*$ relation obtained by van den Bosch (2016). The data are adopted from Table 2 of van den Bosch (2016), in which the BH masses are derived from stellar dynamics, gas dynamics, megamasers, and reverberation mapping. Kormendy & Ho (2013) carefully refined all the present observational data, but only provided an updated $M_{\text{BH}}-\sigma_*$ relation for the galaxies with elliptical and classical bulges. The $M_{\text{BH}}-\sigma_*$ relation for all galaxies with those tabulated data has been given only recently (She et al. 2017). The two formulations of the $M_{\text{BH}}-\sigma_*$ relation for all galaxies obtained both by She et al. (2017) and by van den Bosch (2016) are shown in Figure 10(b) and are nearly identical to each other, justifying the results calculated based on the $M_{\text{BH}}-\sigma_*$ relation obtained by van den Bosch (2016). For comparison, Figure 10(b) also shows several popular $M_{\text{BH}}-\sigma_*$ relations, which are obtained for all types of galaxies (Ferrarese & Ford 2005; McConnell & Ma 2013) and were recently used to estimate the BH masses of TDEs (Stone & Metzger 2016; Blagorodnova et al. 2017; Wevers et al. 2017, 2019b; Leloudas et al. 2019). Figure 10(b) shows that the $M_{\text{BH}}-\sigma_*$ relations for all galaxies are well consistent with one another. The BH masses obtained in this work are located in the core regions of the correlation, with a scatter comparable to the intrinsic scatter of the $M_{\text{BH}}-\sigma_*$ relation. In Figure 10(b), the interpolated $M_{\text{BH}}-\sigma_*$ relation from Equation (26) is also shown and remarkably consistent with those for all types of galaxies in the literature as well as with the BH masses obtained in this work.

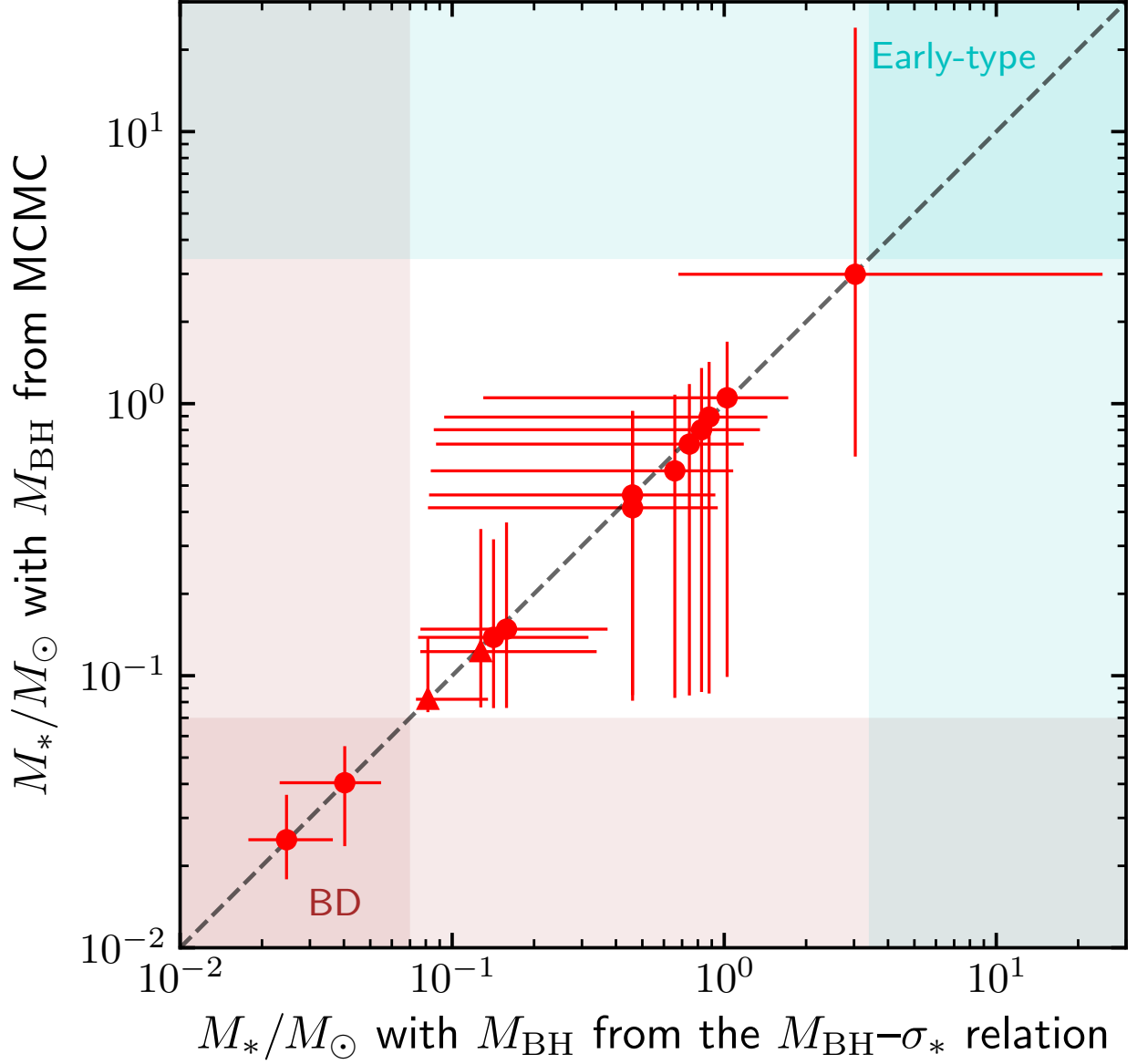


Figure 8. Stellar masses of the sample sources with the BH masses estimated from the MCMC experiments in this paper with those derived from the $M_{\text{BH}}-\sigma_*$ relation of van den Bosch (2016). The filled circles are for the main solutions of TDEs, and the filled triangles are for the secondary solutions. The uncertainties are determined at the 90% confidence level in the MCMC experiments. The stellar masses obtained with the two MCMC experiments are consistent with each other.

In Section 4 we showed observationally and theoretically that the bolometric luminosity and the total radiation energy could properly include the EUV radiation by integrating over a single blackbody from the optical and UV radiation and adding the observations of soft X-ray wave bands. The consistencies of the BH masses obtained in this paper and with the $M_{\text{BH}}-\sigma_*$ relation also suggest that the conclusions are reasonable. However, the spectral energy distributions of a few TDEs occasionally deviate from the single-temperature blackbody spectrum, and the contribution of EUV radiation in the bolometric luminosity and the total radiation energy cannot be well constrained until direct observations of EUV radiation are available. Here we briefly discuss the effects of the EUV radiation on the results by arbitrarily increasing by

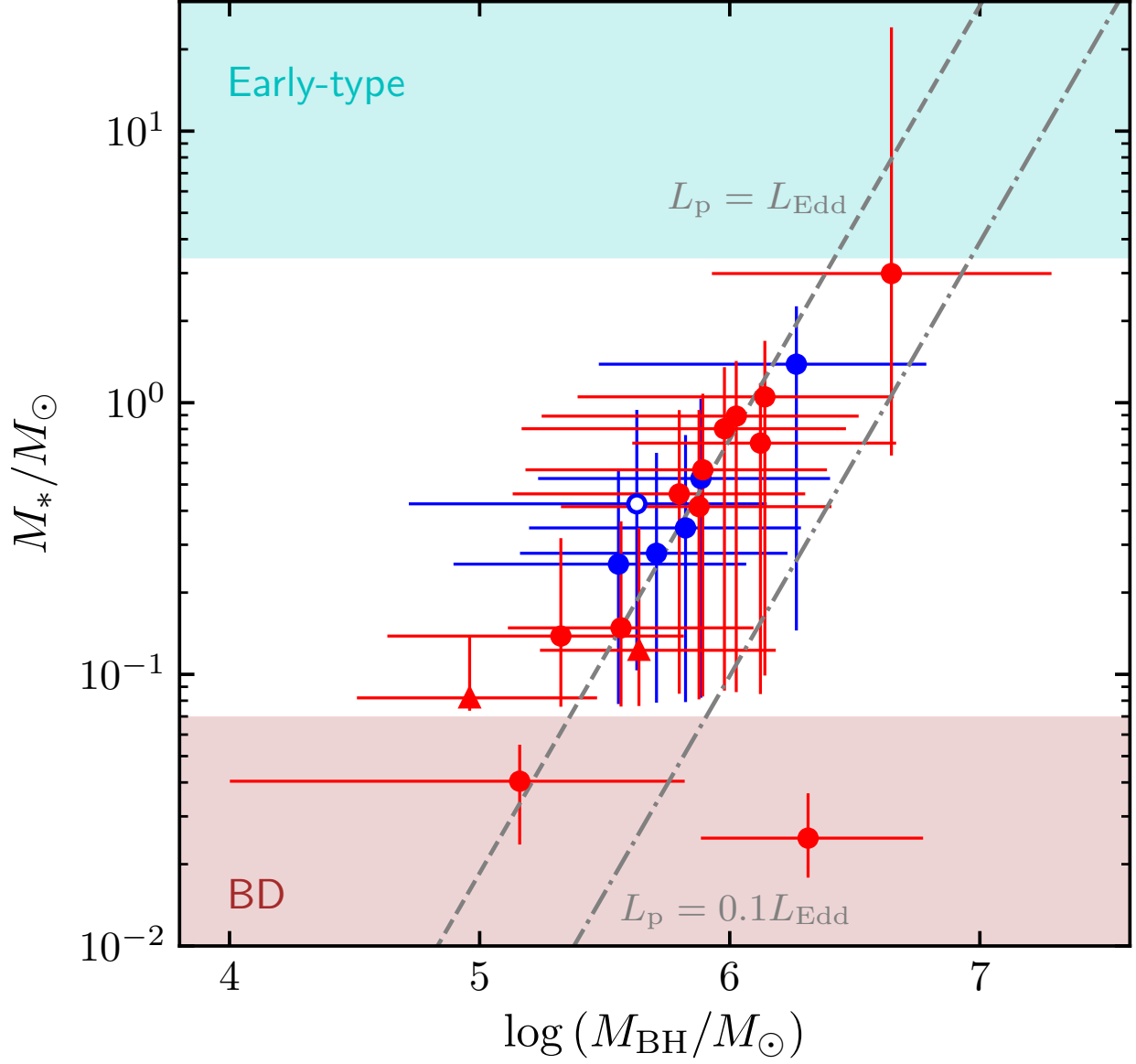


Figure 9. Stellar mass vs. BH mass for all the sample sources derived from our MCMC experiments. The red and blue symbols show the results obtained with and without prior knowledge of the BH mass, respectively. The open circle is the X-ray TDE XMMSL1 J0740, and the filled triangles are for the secondary solutions of iPTF16fnl and GALEXD23H-1. The dashed and dash-dotted lines are the observational limits imposed by Equation (30) for $L_p = L_{\text{Edd}}$ and $0.1 L_{\text{Edd}}$, respectively (see Section 4.3 for details).

0.5 dex the peak bolometric luminosity L_p and the total radiation energy ΔE of the well-known PS1-10jh in Table 1. Such an operation is equivalent to the assumption that the EUV radiation is about 5 times the observed optical/UV radiation and the color index does not significantly change with time. We note that the hypothetical bolometric peak luminosity $L_p = 10^{44.84} \text{ erg s}^{-1}$ is about 11 times the Eddington luminosity for the BH mass $\log(M_{\text{BH}}/M_{\odot}) = 5.71$ given by the $M_{\text{BH}}-\sigma_*$ relation in Table 1, and this luminosity should lead to a top-capped light curve due to the Eddington limit, but this theoretical prediction is inconsistent with the observation of PS1-10jh (Gezari et al. 2012). Here we neglect the inconsistency and investigate the effects of the possibly missed EUV radiation on the results. With the arbitrarily assumed bolometric peak

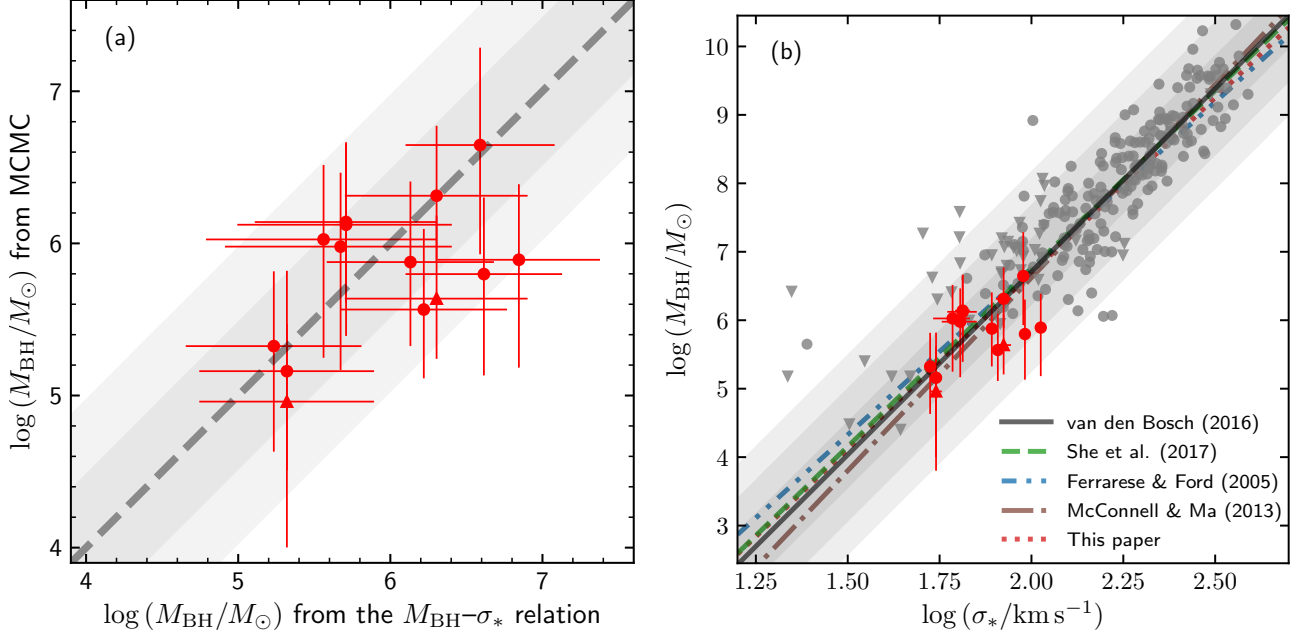


Figure 10. (a) Comparison between the BH mass estimated in this paper with that obtained from the $M_{\text{BH}}-\sigma_*$ relation. The dashed line shows the one-to-one relation, and the dark and light gray regions denote one and two times the intrinsic scatter of the $M_{\text{BH}}-\sigma_*$ relation (van den Bosch 2016). (b) Correlation between BH mass and stellar velocity dispersion. The BH masses obtained in this paper (red points) are overplotted on the $M_{\text{BH}}-\sigma_*$ relation of van den Bosch (2016), which is derived from the data (gray points) in his Table 2. Dark to light gray regions denote one, two, and three times the intrinsic scatter. The lines are the $M_{\text{BH}}-\sigma_*$ relations for all types of galaxies compiled from the literature and the interpolated relation derived in this paper. The BH masses obtained in this paper closely follow the $M_{\text{BH}}-\sigma_*$ relation used in the literature.

luminosity L_p and total radiation energy ΔE , we solve Equations (21) and (23) with the MCMC method. The results suggest a BH mass of $\log(M_{\text{BH}}/M_{\odot}) = 6.39^{+0.74}_{-0.82}$, a stellar mass of $M_*/M_{\odot} = 2.87^{+18.75}_{-2.44}$, and a radiative efficiency of $\log(\eta) = -2.46^{+0.50}_{-0.16}$. These values indicate that a significant increase in EUV radiation from about one to about five times the observed value in optical/UV would increase the radiation efficiency only by 0.11 dex, the BH mass by 0.25 dex, and the mass of the star from $1.05 M_{\odot}$ to $2.87 M_{\odot}$. A star of mass $M_*/M_{\odot} = 2.87$ is an A-type main-sequence star and is roughly consistent with the constraint from the star-formation history of the host galaxy of PS1-10jh (Figure 1 of French et al. 2017). In addition, an increase in peak bolometric luminosity and total radiation energy of PS1-10jh by 0.5 dex would lead to a moderate increase in measured BH mass by 0.25 dex. The BH mass $\log(M_{\text{BH}}/M_{\odot}) = 6.39$ is consistent within 2σ with the BH mass $\log(M_{\text{BH}}/M_{\odot}) = 5.71^{+0.59}_{-0.60}$ obtained with the $M_{\text{BH}}-\sigma_*$ relation. These results imply that the EUV radiation, if significant, would not change our conclusions.

5.2. BH masses from the $M_{\text{BH}}-M_{\text{bulge}}$ relation

In Section 5.1 we computed the BH masses with L_p and ΔE and showed that they are consistent with the BH masses calculated with the $M_{\text{BH}}-\sigma_*$ relation. In addition to the $M_{\text{BH}}-\sigma_*$ relation, the BH masses can also be calculated with the bulge masses M_{bulge} of the host galaxies (Magorrian et al. 1998). The $M_{\text{BH}}-M_{\text{bulge}}$ relation for classical bulges and ellipticals has the same intrinsic scatter as the $M_{\text{BH}}-\sigma_*$ relation (Häring & Rix 2004; Kormendy & Ho 2013). However, it has been noted in the literature that the BH masses of

TDEs derived with the $M_{\text{BH}}-M_{\text{bulge}}$ relations are systematically higher than those obtained with the $M_{\text{BH}}-\sigma_*$ relation (Gezari et al. 2017; Wevers et al. 2017; Mockler et al. 2019), and the BH masses of AGNs are also an order of magnitude lower than those calculated with the $M_{\text{BH}}-M_{\text{bulge}}$ relation. There are several possible explanations for the discrepancy: (1) TDEs are expected to occur in dwarf galaxies and it is difficult to spatially resolve the bulges of the host galaxies, and (2) the host galaxies of most TDEs are E+A galaxies or post-starburst galaxies (Arcavi et al. 2014; French et al. 2016), which are in transition between late-type spirals and passive early-type galaxies and have overdense centers with respect to the galaxies from which the $M_{\text{BH}}-M_{\text{bulge}}$ relation is derived (French et al. 2017). It has recently been suggested that the BH masses of TDEs obtained with the $M_{\text{BH}}-M_{\text{bulge}}$ and $M_{\text{BH}}-\sigma_*$ relations may be roughly consistent with each other when the $M_{\text{BH}}-M_{\text{bulge}}$ relation for all types of host galaxies are used and the B/T ratio is estimated from the total stellar mass and averaged over all types of galaxies (Wevers et al. 2019b). Here we follow this approach to estimate the BH masses. We estimate the B/T ratio for our sample sources using the empirical relation between the total stellar mass of the host galaxy and the averaged B/T obtained for all types of galaxies (Stone et al. 2018). The resulting B/T ratios are given in Table 1 and have very large uncertainties. Following Wevers et al. (2019b), we estimate the BH masses using the $M_{\text{BH}}-M_{\text{bulge}}$ relation for all types of galaxies (Häring & Rix 2004). In Figure 11 we overplot the BH masses obtained with the $M_{\text{BH}}-M_{\text{bulge}}$ relation on the $M_{\text{BH}}-M_{\text{BH}}$ plot. Because it is difficult to estimate the uncertainties of the total stellar masses and the B/T ratios, we only show the uncertainty of the $M_{\text{BH}}-M_{\text{bulge}}$ relation in Figure 11. The real scatter in the BH mass should be larger than what is shown here. Figure 11 shows that the BH masses with the $M_{\text{BH}}-M_{\text{bulge}}$ relation are largely consistent with the BH masses obtained from L_p and ΔE in this paper and from the $M_{\text{BH}}-\sigma_*$ relation, although a small systematic difference is possible.

It is well known that the BHs in quiescent galaxies do not correlate with the galaxy disks (Kormendy & Ho 2013, and references therein). It has recently been shown that the BH masses of local AGNs may correlate with the total stellar mass of the host galaxies M_{tot} (Reines & Volonteri 2015). The relation between BH masses and total stellar masses of the host galaxies of AGNs is used to estimate the BH masses of TDEs in the literature, especially when the stellar velocity dispersion of the host is not available (e.g., Komossa et al. 2004; Gezari et al. 2017; Lin et al. 2017a,b). Using the updated $M_{\text{BH}}-M_{\text{tot}}$ relation (Greene et al. 2020), we calculate the BH masses of the TDE sources with the total stellar masses shown in Table 1 and give the results in Table 1. We overplot the results on the $M_{\text{BH}}-M_{\text{BH}}$ plot in Figure 11. It shows that the BH masses with the $M_{\text{BH}}-M_{\text{tot}}$ relation are well consistent with both the BH masses obtained in this paper and with the $M_{\text{BH}}-\sigma_*$ relation.

5.3. BH masses obtained by fitting the light curves of TDEs

In this paper we propose a method of measuring the masses of BHs and stars of TDEs by jointly fitting the peak bolometric luminosity and the total radiation energy. In the calculations, we use a mass-to-radiation conversion efficiency that is computed from the elliptical disk model suggested by Liu et al. (2017). Mockler et al. (2019) recently proposed measuring the BH masses by fitting the observed light curves of TDEs using the outputs from the numerical simulations of the fallback rate for stellar debris (Guillochon & Ramirez-Ruiz 2013). In their calculations, the conversion efficiency of matter into radiation is assumed to be a free parameter of agnostic physics origin (Mockler et al. 2019).

Figure 12 plots the BH masses obtained in this work and in Mockler et al. (2019). We do not compare the stellar masses because the method of Mockler et al. (2019) cannot constrain the stellar mass due to the strong degeneracy of the stellar mass and the orbital penetration factor. We also plot in Figure 12 the BH masses obtained with the $M_{\text{BH}}-\sigma_*$ relation for comparison. The plot shows that the BH masses obtained

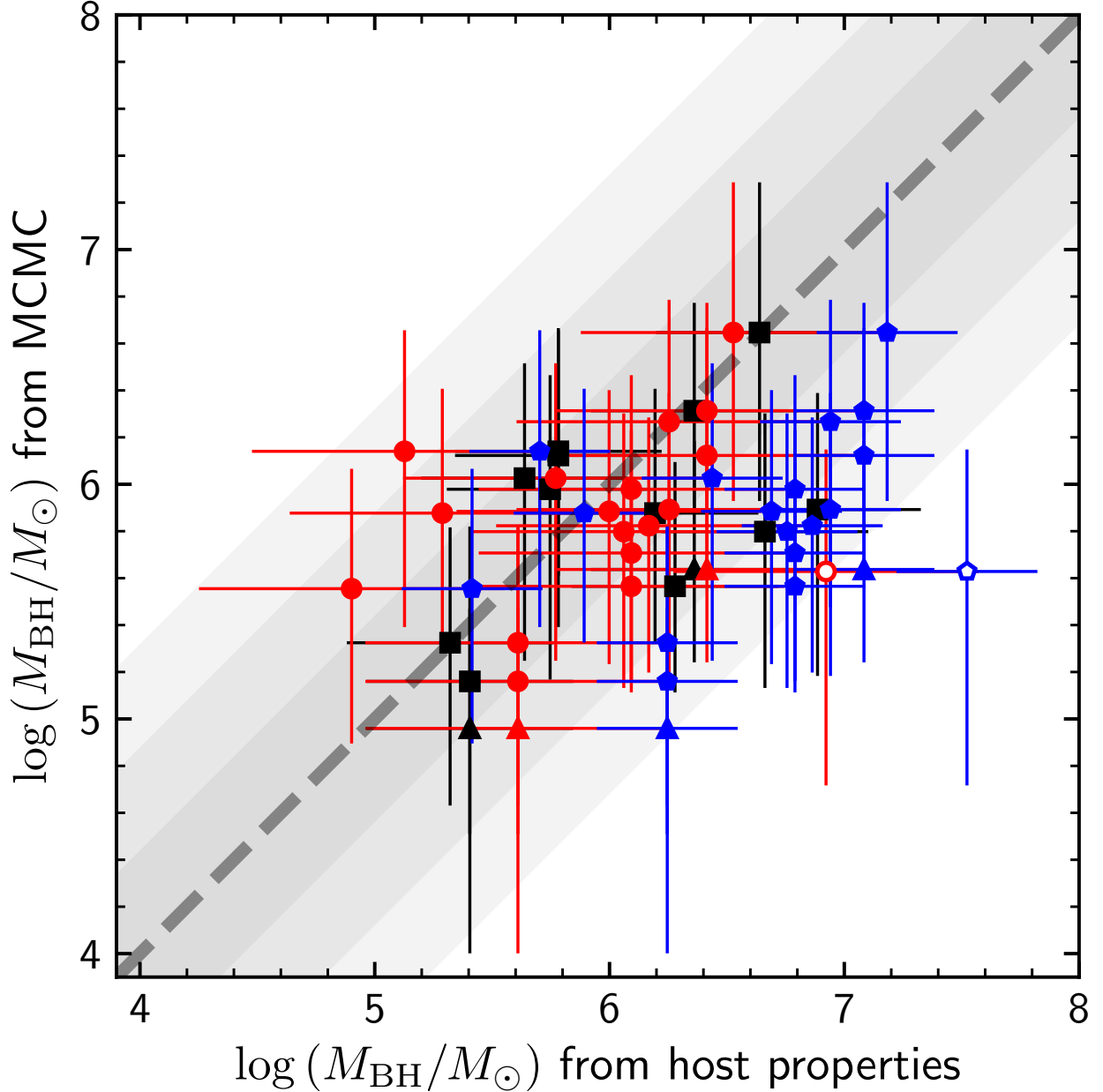


Figure 11. Comparison between the BH masses obtained in this paper with those estimated from the total and bulge masses of the host galaxies. The filled pentagons are obtained with the $M_{\text{BH}}-M_{\text{bulge}}$ relation, while the filled circles come from the $M_{\text{BH}}-M_{\text{tot}}$ relation. The open pentagon and open circle are for the X-ray TDE XMMSL1 J0740. The BH masses calculated with the $M_{\text{BH}}-\sigma_*$ relation (She et al. 2017) are overplotted for comparison as filled squares. The filled triangles are for the secondary solutions of iPTF16fnl and GALEXD23H-1. The dashed line is the one-to-one relation, and the dark to light gray regions give one, two, and three times the intrinsic scatter of the $M_{\text{BH}}-\sigma_*$ relation of She et al. (2017).

by Mockler et al. (2019) are roughly consistent with but systematically higher than those obtained with L_p and ΔE and the $M_{\text{BH}}-\sigma_*$ relation. It has already been noted in the literature that the method of fitting the light curves systematically produces higher BH masses than the $M_{\text{BH}}-\sigma_*$ relation (Mockler et al. 2019). Of all the sample sources, GALEX D1-9 is the most controversial because the BH masses derived from the

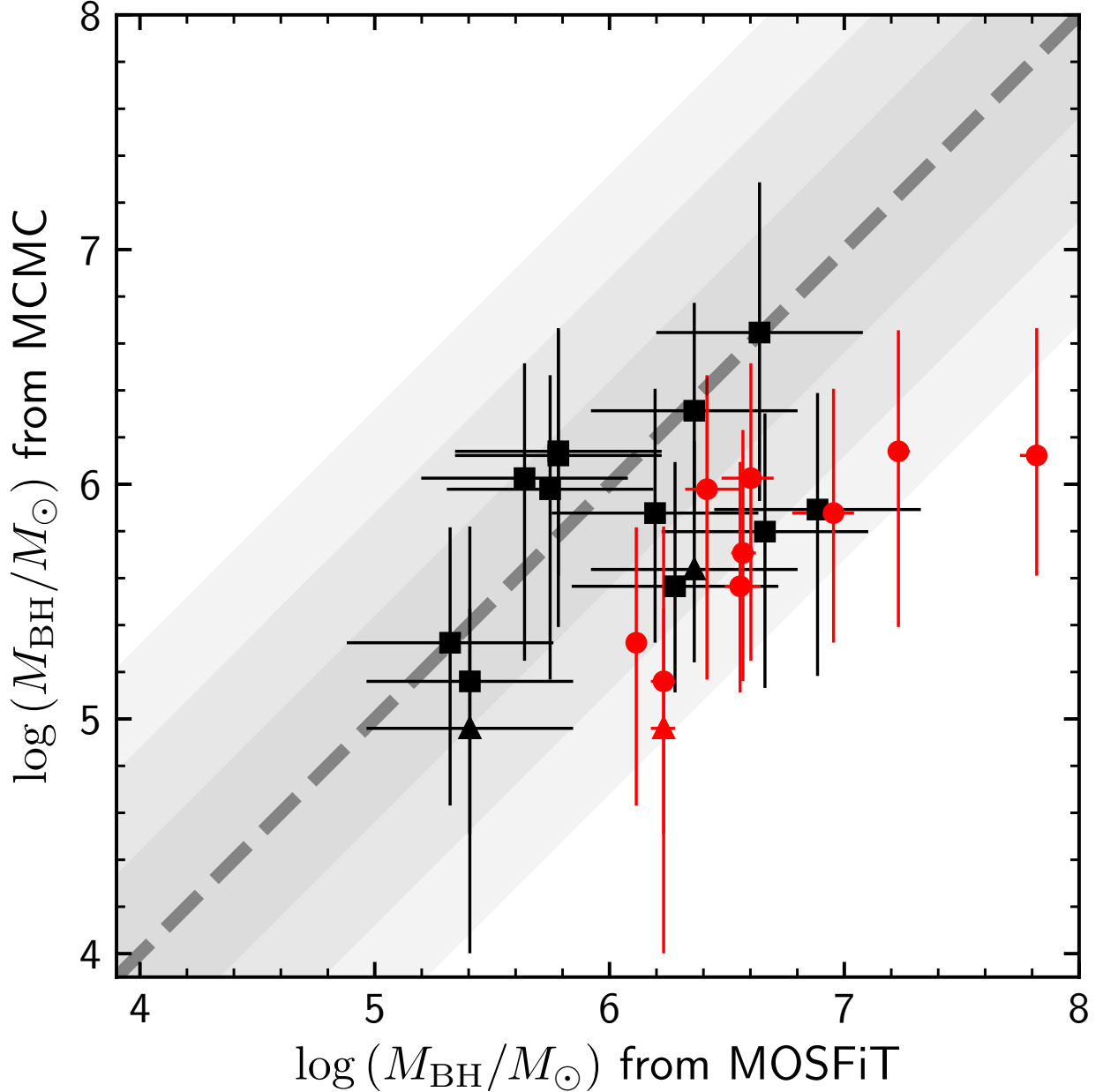


Figure 12. Comparison of the BH masses obtained in this paper with those derived by fitting the multiwavelength light curves of TDEs (Mockler et al. 2019). BH masses calculated with the $M_{\text{BH}}-\sigma_*$ relation (She et al. 2017) are overplotted for comparison as filled squares. The dashed line is the one-to-one relation, and the dark to light gray regions give one, two, and three times the intrinsic scatter of the $M_{\text{BH}}-\sigma_*$ relation of She et al. (2017).

three methods are very different. The light curve of GALEX D1-9 suggests a BH mass about $6.6 \times 10^7 M_\odot$ (Mockler et al. 2019), which is about two orders of magnitude larger than that ($10^{5.71} M_\odot$) obtained with the $M_{\text{BH}}-\sigma_*$ relation and about fifty times larger than the result $10^{6.12} M_\odot$ of this paper.

6. DISCUSSION

Liu and collaborators recently suggested that the accretion disks of TDEs are extended and highly eccentric with nearly uniform eccentricity. The nearly constant orbital eccentricity of the disk fluid elements

during the accretion onto the BH could explain the complex profiles of the observed emission lines (Liu et al. 2017; Cao et al. 2018). Here we calculated the radiation efficiency of the elliptical accretion disk model. Our results show that the radiation efficiency of the highly eccentric accretion disk depends on the masses of the BHs and stars as well as on the orbital penetration factors of the stars. The values could significantly vary with TDEs. The radiation efficiency of the elliptical accretion disk model could be as low as 10^{-3} , or about two orders of magnitude lower than the typical radiation efficiency $\eta = 0.1$ adopted for TDEs in the literature. Based on the elliptical accretion disk model, we calculate the expected peak luminosity and total radiation energy after peak, which can be well determined by observations of TDEs.

We compile from the literature the observational data of the peak bolometric luminosities and total radiation energies after peak for a sample of 18 non-jetted TDEs in quiescent galaxies. Twelve of these TDEs have available stellar velocity dispersions from the observations of their host galaxies, so that the BH masses can be calculated from the $M_{\text{BH}}-\sigma_*$ relation. We show that the peak bolometric luminosities and the total radiation energies computed from the elliptical disk model are consistent with the observational data. The low peak luminosity and apparently low accreted mass could be explained by the unusually low radiation efficiency of elliptical accretion disks without requiring alternative explanations for the transient sources (e.g., Saxton et al. 2018) or missing the majority of the released energy in the EUV (e.g., Lu & Kumar 2018).

Given L_p and ΔE , we can calculate the radiation efficiency and determine the mass of the disrupted star through Equations (21) and (23) using the MCMC experiments, regardless of a prior knowledge of the BH mass. Our sample sources except for GALEX D23H-1 have a typical radiation efficiency $\eta \simeq 2.7 \times 10^{-3}$, which is about 37 times lower than the typical radiation efficiency $\eta = 0.1$ adopted for TDEs in the literature. Our results are consistent with those from earlier work. The radiation efficiency of PTF09djl and ASASSN-14li are $\log \eta = -2.61_{-0.10}^{+0.58}$ and $\log \eta = -2.57_{-0.14}^{+0.54}$, respectively. These values are consistent with the results $\log \eta \simeq -2.38$ for PTF09djl and $\log \eta \simeq -2.43$ for ASASSN-14li, obtained by modeling the profiles of the broad optical emission lines (Liu et al. 2017; Cao et al. 2018). The radiation efficiencies of a sample of TDEs have recently been obtained by fitting the light curves with the fallback rate of stellar debris (MOSFiT, Mockler et al. 2019). However, the uncertainties of the MOSFiT results are very large because the radiation efficiency from the MOSFiT method is strongly degenerate with stellar masses ranging from $0.01 M_\odot$ to $100 M_\odot$ and cannot be determined uniquely. As an example, Table 5 of Mockler et al. (2019) gave the radiation efficiencies of TDE PS1-10jh obtained with different stellar masses. They showed that the values change from $\eta = 0.9 \times 10^{-1}$ for $M_* = 0.1 M_\odot$, through $\eta = 3.8 \times 10^{-3}$ for $M_* = 1.0 M_\odot$, to $\eta = 4 \times 10^{-4}$ for $M_* = 10 M_\odot$. No strong prior can be given to the stellar mass, and the uncertainty is as large as 3 dex. This uncertainty is much larger than the quoted uncertainty of the fiducial value $\eta = 0.09_{-0.02}^{+0.03}$ (Mockler et al. 2019). In this paper, the stellar mass and radiative efficiency of the TDE PS1-10jh can be determined separately. The results are shown in Table 2, which are $M_* = 1.02_{-0.89}^{+0.69} M_\odot$ and $\log(\eta) = -2.55_{-0.13}^{+0.68}$. Our result is significantly smaller than the fiducial one from the MOSFiT method. Interestingly, our result is consistent with the test result of $M_* = 1.0 M_\odot$ and $\eta = 3.8 \times 10^{-3}$ (or $\log \eta = -2.42$) of the MOSFiT method. Taking into account that the systematic uncertainty of the result of the MOSFiT method is large, we conclude that the radiation efficiencies obtained in this paper are consistent with those from the MOSFiT method.

To produce the same total radiation energy, a low radiation efficiency requires a large amount of accreted matter onto the BH. We calculated the amount of accreted stellar matter after peak and showed that it is in the range of about $10^{-2} M_\odot$ to $0.97 M_\odot$, about 34% of the mass of the star. The fraction of 34% is the expectation of hydrodynamic simulations of tidal disruption of low-mass stars with a polytropic index

$\gamma = 5/3$ and orbital penetration factor $\beta \sim 1$. Our model is unable to constrain the accreted matter before the peak, and we cannot estimate the total accreted stellar matter of TDEs. The results imply that most of the orbital energy of the stellar debris is advected onto the BH instead of being converted into radiation in the EUV, which last is often assumed in the literature (e.g., [Lu & Kumar 2018](#)). In addition, because of the low peak bolometric luminosity and total radiation energy as well as the apparently low accreted matter of the optical/UV nuclear transients, we do not require an alternative explanation, as suggested in [Saxton et al. \(2018\)](#).

We also find that the disrupted stars of our TDE sample except SDSS J0952+2143 are in the mass range of $M_* \simeq 2.5 \times 10^{-2} M_\odot$ and $1.4 M_\odot$. The spectral types range from brown dwarfs to late A-type main sequence. The absence of B- and O-type stars in our sample is consistent with the observational fact that the host galaxies of many TDEs are E+A galaxies with a burst of star formation about a few billion years ago ([Arcavi et al. 2014](#); [French et al. 2016](#)). The stellar mass of the TDE in SDSS J0952+2143 is about $3.0 M_\odot$ and consistent with the fact that the host galaxy of SDSS J0952+2143 is a star-forming galaxy ([Komossa et al. 2008](#)) rich in young stars ([Palaversa et al. 2016](#)).

With the peak bolometric luminosity and the total radiation energy after peak, we can constrain the masses of the BHs of TDEs. The BH masses obtained in this paper are consistent with those obtained with the classical $M_{\text{BH}}-\sigma_*$, $M_{\text{BH}}-M_{\text{bulge}}$, and $M_{\text{BH}}-M_{\text{tot}}$ relations. It was noted in the literature that the BH masses of TDEs given with the $M_{\text{BH}}-L_{\text{bulge}}$ or $M_{\text{BH}}-M_{\text{bulge}}$ relation are much higher than those calculated with the $M_{\text{BH}}-\sigma_*$ relation. Our results suggest that the discrepancy is most probably due to the difficulty of accurately measuring the mass of the host galaxy bulge.

The BH masses of many of our sample TDE sources have recently been calculated with the MOSFiT method, which is based on analyzing the multiwave-band light curves ([Mockler et al. 2019](#)). The BH masses of the TDEs obtained in this paper and with MOSFiT are largely consistent with each other, with some exceptions. For GALEX D1-9 and PS1-10jh, the MOSFiT method gives $M_{\text{BH}} = 6.6 \times 10^7 M_\odot$ and $M_{\text{BH}} = 1.7 \times 10^7 M_\odot$, respectively, which is about 50 times and 12 times higher, respectively, than our results. It has also been noted in the original work ([Mockler et al. 2019](#)) and in this paper that the measurements of the BH masses of GALEX D1-9 and TDE PS1-10jh with MOSFiT are much higher than the measurement of $10^{5.71} M_\odot$ calculated with the $M_{\text{BH}}-\sigma_*$ relation. The BH mass in the MOSFiT method is determined under the assumption that the bound debris is promptly circularized, so that the luminosity closely follows the mass fallback rate without significant delay ([Mockler et al. 2019](#)). A prompt circularization of stellar debris streams and the rapid formation of an accretion disk are expected only for tidal disruptions of the stars with an orbital pericenter of about the gravitational radius of the BH ([Dai et al. 2015](#); [Shiokawa et al. 2015](#); [Bonnerot et al. 2016](#); [Hayasaki et al. 2016](#)). The circularization of debris streams is slow for BHs of mass $\sim 10^6 M_\odot$ and a typical penetration factor $\beta \sim 1$ because the general relativistic apsidal precession is weak. An inefficient circularization of stellar debris would result in a rise-to-peak timescale longer than that given by Δt_p . A direct comparison of the observed rise-to-peak timescale and the expected Δt_p would require a more massive BH solution of the MOSFiT method.

Twelve of the 18 TDEs in our sample have stellar velocity dispersions measured from the host galaxies. When the BH masses obtained in this paper are plotted on the $M_{\text{BH}}-\sigma_*$ diagram with the BH masses measured by the stellar dynamics, gas dynamics, megamasers, and reverberation mapping, we find that they share the same $M_{\text{BH}}-\sigma_*$ relation and that the BH masses in our sample distribute in the low-mass region of the $M_{\text{BH}}-\sigma_*$ diagram. The results indicate that the method in this paper can give an independent accurate measurement of the BH mass and test the $M_{\text{BH}}-\sigma_*$ relation at low BH mass. We have calculated the BH

masses of the 6 sample TDEs without measuring the stellar velocity dispersions of the host galaxies. It would be interesting to compare these masses with those derived in the future from the $M_{\text{BH}}-\sigma_*$ relation.

The masses of the BHs and the tidally disrupted stars obtained in this paper are determined mainly by the absolute peak brightness and the total radiation energy integrated over the light curve after peak. The results depend very weakly on either the shapes of the light curves or the properties of the stars. The consistency between the BH masses obtained in this paper and those from the $M_{\text{BH}}-\sigma_*$ relation, as well as the agreement between the accreted stellar masses derived from our model and those from the hydrodynamical simulations, justifies the elliptical accretion disk model of large size and invariant extreme eccentricity (Liu et al. 2017; Cao et al. 2018). Such a disk usually has a sub-Eddington luminosity for the BHs of mass $\gtrsim 10^6 M_\odot$ and is significantly super-Eddington only for tidal disruption of main-sequence stars by intermediate-mass BHs with mass $M_{\text{BH}} \lesssim 10^5 M_\odot$. An accretion disk of sub-Eddington luminosity is cool and radiatively efficient, and the luminosity closely follows the fallback rate of the stellar debris. The radiation energy of the elliptical accretion disk model is consistent with the observations, and no optically thick envelope is needed. No strong disk wind or outflow is expected to form on the surface of the cool sub-Eddington accretion disk. However, a small fraction of the fallback matter may become unbound and form outflows due to the shocks when the streams collide at the apocenter of the elliptical disk (Jiang et al. 2016). In this case, absorption lines may be detected in the spectrum.

7. CONCLUSIONS

We have calculated the radiation efficiency for a sample of TDEs based on the elliptical accretion disk model and investigated its implications for the observations of TDEs. We showed that the low peak bolometric luminosity and low total radiation energy of TDEs result from the low radiation efficiency of the elliptical accretion disk and that the main radiation comes from the disk rather than from the self-crossing shocks at apocenter. When the peak bolometric luminosity and the total radiation energy after peak are known, we can derive the masses of the BHs and stars.

Since the method in this paper does not require the knowledge of the properties of the host galaxies, it can also be used to measure the masses of off-center recoiling BHs or a component of supermassive BH pairs in galaxy mergers, the masses of intermediate-mass BHs in globular star clusters, or the masses of primordial BHs wandering in galactic disks or halos. This alternative method for estimating the BH mass is also important for classical galaxies with central supermassive BHs because (1) in dwarf galaxies, accurate σ_* measurements require deep exposures with very high spectral resolution, (2) measuring σ_* becomes more difficult for high- z sources, and (3) upcoming and next-generation sky surveys are expected to detect thousands of TDEs, making spectroscopic follow-ups of all these sources extremely challenging. Finally, we would like to emphasize again that the BH-galaxy scaling relationship below a BH mass of $\sim 10^6 M_\odot$ has not been fully explored in the past. TDEs offer a rare opportunity to probe this unexplored regime, as has been demonstrated in this work.

ACKNOWLEDGEMENTS

We would like to thank Hua Gao, Julian Krolik, Nadejda Blagorodnova, Richard Saxton, and Thomas Wevers for helpful discussions. We are grateful to the anonymous referee for very helpful comments. This work is supported by the National Natural Science Foundation of China (NSFC No.11473003, NSFC No.11721303) and the Strategic Priority Research Program of the Chinese Academy of Sciences (grant No. XDB23010200 and No. XDB23040000). L.C.H was supported by the National Key R&D Program of

China (2016YFA0400702). X.C. acknowledged the support of the National Natural Science Foundation of China (NSFC No.11991053)

Software: Astropy (Astropy Collaboration et al. 2013), emcee (Foreman-Mackey et al. 2013), Imfit (Newville et al. 2014), Matplotlib (Hunter 2007), NumPy (Harris et al. 2020), Pandas (McKinney 2010) and SciPy (Virtanen et al. 2020).

REFERENCES

- Abramowicz, M. A., Czerny, B., Lasota, J. P., & Szuszkiewicz, E. 1988, *ApJ*, 332, 646
- Abramowicz, M. A., Jaroszynski, M., & Sikora, M. 1978, *A&A*, 63, 221
- Andalman, Z.L., Liska, M.T. P., Tchekhovskoy, A., Coughlin, E.R., & Stone, N. 2020, *MNRAS*, submitted (arXiv:2008.04922)
- Arcavi, I., Gal-Yam, A., Sullivan, M., et al. 2014, *ApJ*, 793, 38
- Astropy Collaboration, Robitaille, T. P., Tollerud, E. J., et al. 2013, *A&A*, 558, A33
- Barker, A. J., & Ogilvie, G. I. 2016, *MNRAS*, 458, 3739
- Bell, E. F., McIntosh, D. H., Katz, N., & Weinberg, M. D. 2003, *ApJS*, 149, 289
- Blagorodnova, N., Cenko, S. B., Kulkarni, S. R., et al. 2019, *ApJ*, 873, 92
- Blagorodnova, N., Gezari, S., Hung, T., et al. 2017, *ApJ*, 844, 46
- Bogdanović, T., Eracleous, M., Mahadevan, S., Sigurdsson, S., & Laguna, P. 2004, *ApJ*, 610, 707
- Bonnerot, C., & Lu, W. 2020, *MNRAS*, 495, 1374
- Bonnerot, C., Rossi, E. M., & Lodato, G. 2017, *MNRAS*, 464, 2816
- Bonnerot, C., Rossi, E. M., Lodato, G., & Price, D. J. 2016, *MNRAS*, 455, 2253
- Bright, J. S., Fender, R. P., Motta, S. E., et al. 2018, *MNRAS*, 475, 4011
- Brown, J. S., Holoien, T. W.-S., Auchettl, K., et al. 2017, *MNRAS*, 466, 4904
- Brown, J. S., Kochanek, C. S., Holoien, T. W.-S., et al. 2018, *MNRAS*, 473, 1130
- Cao, R., Liu, F. K., Zhou, Z. Q., Komossa, S., & Ho, L. C. 2018, *MNRAS*, 480, 2929
- Cappelluti, N., Ajello, M., Rebusco, P., et al. 2009, *A&A*, 495, L9
- Chabrier, G., & Baraffe, I. 2000, *ARA&A*, 38, 337
- Chan, C.-H., Krolik, J. H., & Piran, T. 2018, *ApJ*, 856, 12
- Chen, K., & Halpern, J. P. 1989, *ApJ*, 344, 115
- Chen, K., Halpern, J. P., & Filippenko, A. V. 1989, *ApJ*, 339, 742
- Chen, X., Liu, F. K., & Magorrian, J. 2008, *ApJ*, 676, 54
- Chen, X., Madau, P., Sesana, A., & Liu, F. K. 2009, *ApJL*, 697, L149
- Chornock, R., Berger, E., Gezari, S., et al. 2014, *ApJ*, 780, 44
- Coughlin, E.R., & Nixon, C.J. 2019, *ApJL*, 883, L17
- Cox, A. N. 2000, *Allen's Astrophysical Quantities* (New York: Springer)
- Dai, L., McKinney, J. C., & Miller, M. C. 2015, *ApJL*, 812, L39
- Dai, L., McKinney, J. C., Roth, N., Ramirez-Ruiz, E., & Miller, M. C. 2018, *ApJL*, 859, L20
- Darbha, S., Coughlin, E. R., Kasen, D., & Nixon, C. 2019, *MNRAS*, 488, 5267
- Donato, D., Cenko, S. B., Covino, S., et al. 2014, *ApJ*, 781, 59
- Eracleous, M., & Halpern, J. P. 1994, *ApJS*, 90, 1
- Eracleous, M., & Halpern, J. P. 2003, *ApJ*, 599, 886
- Esquej, P., Saxton, R. D., Komossa, S., et al. 2008, *A&A*, 489, 543
- Evans, C., Laguna, P., & Eracleous, M. 2015, *ApJL*, 805, L19
- Evans, C. R., & Kochanek, C. S. 1989, *ApJL*, 346, L13
- Ferrarese, L., & Ford, H. 2005, *SSRv*, 116, 523
- Foreman-Mackey, D., Hogg, D. W., Lang, D., & Goodman, J. 2013, *PASP*, 125, 306
- French, K. D., Arcavi, I., & Zabludoff, A. 2016, *ApJL*, 818, L21
- French, K. D., Arcavi, I., & Zabludoff, A. 2017, *ApJ*, 835, 176
- Gezari, S., Basa, S., Martin, D. C., et al. 2008, *ApJ*, 676, 944
- Gezari, S., Cenko, S. B., & Arcavi, I. 2017, *ApJL*, 851, L47

- Gezari, S., Chornock, R., Rest, A., et al. 2012, *Nature*, 485, 217
- Gezari, S., Heckman, T., Cenko, S. B., et al. 2009, *ApJ*, 698, 1367
- Gezari, S., Martin, D. C., Milliard, B., et al. 2006, *ApJL*, 653, L25
- Goicovic, F. G., Springel, V., Ohlmann, S. T., & Pakmor, R. 2019, *MNRAS*, 487, 981
- Golightly, E. C. A., Nixon, C. J., & Coughlin, E. R. 2019, *ApJL*, 882, L26
- Graur, O., French, K. D., Zahid, H. J., et al. 2018, *ApJ*, 853, 39
- Greene, J.E., Strader, J., & Ho, L.C. 2020, *ARA&A*, 58, 257
- Guillochon, J., Manukian, H., & Ramirez-Ruiz, E. 2014, *ApJ*, 783, 23
- Guillochon, J., & Ramirez-Ruiz, E. 2013, *ApJ*, 767, 25
- Halpern, J. P., Gezari, S., & Komossa, S. 2004, *ApJ*, 604, 572
- Häring, N., & Rix, H.-W. 2004, *ApJL*, 604, L89
- Harris, C. R., Millman, K. J., van der Walt, S. J., et al. 2020, *Nature*, 585, 357
- Hayasaki, K., Stone, N., & Loeb, A. 2013, *MNRAS*, 434, 909
- Hayasaki, K., Stone, N., & Loeb, A. 2016, *MNRAS*, 461, 3760
- Hills, J. G. 1975, *Nature*, 254, 295
- Ho, L. C., Rudnick, G., Rix, H.-W., et al. 2000, *ApJ*, 541, 120
- Holoien, T. W.-S., Brown, J. S., Auchettl, K., et al. 2018, *MNRAS*, 480, 5689
- Holoien, T. W.-S., Huber, M. E., Shappee, B. J., et al. 2019a, *ApJ*, 880, 120
- Holoien, T. W.-S., Kochanek, C. S., Prieto, J. L., et al. 2016a, *MNRAS*, 455, 2918
- Holoien, T. W.-S., Kochanek, C. S., Prieto, J. L., et al. 2016b, *MNRAS*, 463, 3813
- Holoien, T. W.-S., Prieto, J. L., Bersier, D., et al. 2014, *MNRAS*, 445, 3263
- Holoien, T. W. S., Vallely, P. J., Auchettl, K., et al. 2019b, *ApJ*, 883, 111
- Hung, T., Cenko, S. B., Roth, N., et al. 2019, *ApJ*, 879, 119
- Hung, T., Gezari, S., Blagorodnova, N., et al. 2017, *ApJ*, 842, 29
- Hunter, J. D. 2007, *Computing in Science and Engineering*, 9, 90
- Jiang, Y.-F., Guillochon, J., & Loeb, A. 2016, *ApJ*, 830, 125
- Jonker, P. G., Stone, N. C., Generozov, A., van Velzen, S., & Metzger, B. 2020, *ApJ*, 889, 166
- Kippenhahn, R., Weigert, A., & Weiss, A. 2012, *Stellar Structure and Evolution* (Berlin: Springer-Verlag)
- Kochanek, C. S. 1994, *ApJ*, 422, 508
- Kochanek, C. S. 2016, *MNRAS*, 461, 371
- Komossa, S. 2015, *Journal of High Energy Astrophysics*, 7, 148
- Komossa, S., & Bade, N. 1999, *A&A*, 343, 775
- Komossa, S., Halpern, J., Schartel, N., et al. 2004, *ApJL*, 603, L17
- Komossa, S., Zhou, H., Wang, T., et al. 2008, *ApJL*, 678, L13
- Kormendy, J., & Ho, L. C. 2013, *ARA&A*, 51, 511
- Kuin, N. P. M., Wu, K., Oates, S., et al. 2019, *MNRAS*, 487, 2505
- Law-Smith, J., Guillochon, J., & Ramirez-Ruiz, E. 2019, *ApJL*, 882, L25
- Law-Smith, J., Ramirez-Ruiz, E., Ellison, S. L., & Foley, R. J. 2017, *ApJ*, 850, 22
- Leloudas, G., Dai, L., Arcavi, I., et al. 2019, *ApJ*, 887, 218
- Li, L.-X., Narayan, R., & Menou, K. 2002, *ApJ*, 576, 753
- Li, S., Liu, F. K., Berczik, P., & Spurzem, R. 2017, *ApJ*, 834, 195
- Lin, D., Godet, O., Ho, L. C., et al. 2017a, *MNRAS*, 468, 783
- Lin, D., Guillochon, J., Komossa, S., et al. 2017b, *Nature Astronomy*, 1, 0033
- Liu, F. K., Cao, C. Y, Abramowicz, M. A., et al. 2020, *ApJ*, accepted (arXiv:2012.05552)
- Liu, F. K., & Chen, X. 2013, *ApJ*, 767, 18
- Liu, F. K., Li, S., & Komossa, S. 2014, *ApJ*, 786, 103
- Liu, F. K., Zhou, Z. Q., Cao, R., Ho, L. C., & Komossa, S. 2017, *MNRAS*, 472, L99
- Lodato, G., King, A. R., & Pringle, J. E. 2009, *MNRAS*, 392, 332
- Lodato, G., & Rossi, E. 2011, *MNRAS*, 410, 359
- Lu, W., & Kumar, P. 2018, *ApJ*, 865, 128
- Magorrian, J., & Tremaine, S. 1999, *MNRAS*, 309, 447
- Magorrian, J., Tremaine, S., Richstone, D., et al. 1998, *AJ*, 115, 2285
- Maksym, W. P., Ulmer, M. P., & Eracleous, M. 2010, *ApJ*, 722, 1035
- Margutti, R., Metzger, B. D., Chornock, R., et al. 2019, *ApJ*, 872, 18
- McConnell, N. J., & Ma, C.-P. 2013, *ApJ*, 764, 184

- McKinney, W., Data Structures for Statistical Computing in Python, in Proc. of the 9th Python in Science Conf.(SciPy 2010), ed. van der Walt, S. & Millman, J., 51
- Metzger, B.D., & Stone, N.C. 2016, MNRAS, 461, 948
- Miller, J. M., Kaastra, J. S., Miller, M. C., et al. 2015, Nature, 526, 542
- Mockler, B., Guillochon, J., & Ramirez-Ruiz, E. 2019, ApJ, 872, 151
- Nealon, R., Price, D.J., Bonnerot, C., & Lodato, G. 2018, MNRAS, 474, 1737
- Newville, M., Stensitzki, T., Allen, D. B., & Ingargiola, A. 2014, LMFIT: Non-Linear Least-Square Minimization and Curve-Fitting for Python, 0.8.0, Zenodo
- Nicholl, M., Blanchard, P. K., Berger, E., et al. 2019, MNRAS, 488, 1878
- Ogilvie, G. I., & Lynch, E. M. 2019, MNRAS, 483, 4453
- Onori, F., Cannizzaro, G., Jonker, P. G., et al. 2019, MNRAS, 489, 1463
- Paczynski, B. 1980, AcA, 30, 347
- Palaversa, L., Gezari, S., Sesar, B., et al. 2016, ApJ, 819, 151
- Papaloizou, J. C. B., & Pringle, J. E. 1984, MNRAS, 208, 721
- Perley, D. A., Mazzali, P. A., Yan, L., et al. 2019, MNRAS, 484, 1031
- Piran, T., Svirski, G., Krolik, J., Cheng, R. M., & Shiokawa, H. 2015, ApJ, 806, 164
- Popović, L. Č., Mediavilla, E., Bon, E., & Ilić, D. 2004, A&A, 423, 909
- Rees, M. J. 1988, Nature, 333, 523
- Reines, A. E., & Volonteri, M. 2015, ApJ, 813, 82
- Rosswog, S., Ramirez-Ruiz, E., & Hix, W. R. 2009, ApJ, 695, 404
- Roth, N., Kasen, D., Guillochon, J., & Ramirez-Ruiz, E. 2016, ApJ, 827, 3
- Ryu, T., Krolik, J., Piran, T., & Noble, S. C. 2020a, ApJ, 904, 98
- Ryu, T., Krolik, J., Piran, T., & Noble, S. C. 2020b, ApJ, 904, 99
- Ryu, T., Krolik, J., Piran, T., & Noble, S. C. 2020c, ApJ, 904, 100
- Sądowski, A., Tejada, E., Gafton, E., Rosswog, S., & Abarca, D. 2016, MNRAS, 458, 4250
- Saxton, C. J., Perets, H. B., & Baskin, A. 2018, MNRAS, 474, 3307
- Saxton, R. D., Read, A. M., Komossa, S., et al. 2017, A&A, 598, A29
- Saxton, R. D., Read, A. M., Komossa, S., et al. 2019, A&A, 630, A98
- She, R., Ho, L. C., & Feng, H. 2017, ApJ, 835, 223
- Shields, J. C., Rix, H.-W., McIntosh, D. H., et al. 2000, ApJ, 534, L27
- Shiokawa, H., Krolik, J. H., Cheng, R. M., Piran, T., & Noble, S. C. 2015, ApJ, 804, 85
- Stone, N., Sari, R., & Loeb, A. 2013, MNRAS, 435, 1809
- Stone, N. C., Generozov, A., Vasiliev, E., & Metzger, B. D. 2018, MNRAS, 480, 5060
- Stone, N. C., & Metzger, B. D. 2016, MNRAS, 455, 859
- Storchi-Bergmann, T., Baldwin, J. A., & Wilson, A. S. 1993, ApJL, 410, L11
- Storchi-Bergmann, T., Schimoia, J. S., Peterson, B. M., et al. 2017, ApJ, 835, 236
- Strateva, I. V., Strauss, M. A., Hao, L., et al. 2003, AJ, 126, 1720
- Strubbe, L. E., & Quataert, E. 2009, MNRAS, 400, 2070
- Svirski, G., Piran, T., & Krolik, J. 2017, MNRAS, 467, 1426
- Tejada, E., & Rosswog, S. 2013, MNRAS, 433, 1930
- van den Bosch, R. C. E. 2016, ApJ, 831, 134
- van Velzen, S. 2018, ApJ, 852, 72
- van Velzen, S., Farrar, G. R., Gezari, S., et al. 2011, ApJ, 741, 73
- van Velzen, S., Gezari, S., Cenko, S. B., et al. 2019a, ApJ, 872, 198
- van Velzen, S., Gezari, S., Hammerstein, E., et al. 2020, ApJ, in press (arXiv:2001.01409)
- van Velzen, S., Stone, N. C., Metzger, B. D., et al. 2019b, ApJ, 878, 82
- Vinkó, J., Yuan, F., Quimby, R. M., et al. 2015, ApJ, 798, 12
- Virtanen, P., Gommers, R., Oliphant, T. E., et al. 2020, Nature Methods, 17, 261
- Wang, J., & Merritt, D. 2004, ApJ, 600, 149
- Wang, T.-G., Zhou, H.-Y., Komossa, S., et al. 2012, ApJ, 749, 115
- Wevers, T., Pasham, D. R., van Velzen, S., et al. 2019a, MNRAS, 488, 4816
- Wevers, T., Stone, N. C., van Velzen, S., et al. 2019b, MNRAS, 487, 4136
- Wevers, T., van Velzen, S., Jonker, P. G., et al. 2017, MNRAS, 471, 1694